

# The recent star formation histories of nearby galaxies on resolved scales

Maria Lomaeva,<sup>1\*</sup> Amélie Saintonge,<sup>1</sup> Ilse De Looze,<sup>1,2</sup>

<sup>1</sup>*Dept. of Physics & Astronomy, University College London, Gower Street, London WC1E 6BT, UK*

<sup>2</sup>*Sterrenkundig Observatorium, Ghent University, Krijgslaan 281 - S9, 9000 Gent, Belgium*

Accepted XXX. Received YYY; in original form ZZZ

## ABSTRACT

Star formation histories (SFHs) of galaxies are affected by a variety of factors, both external (field vs. cluster/group) and internal (presence of a bar and AGN, morphological type). In this work, we extend our previous study and apply the  $\langle SFR_5 \rangle / \langle SFR_{200} \rangle$  metric to a sample of eleven nearby galaxies with MUSE observations. Based on a combination of H $\alpha$  and UV photometry,  $\langle SFR_5 \rangle / \langle SFR_{200} \rangle$  is sensitive to star formation timescales of  $\sim 5$ –200 Myr and therefore measures the present-day rate of change in the star formation rate, dSFR/dt. Within this limited galaxy sample, we do not observe systematic variations between the global value of  $\langle SFR_5 \rangle / \langle SFR_{200} \rangle$  and the presence of an active galactic nucleus, stellar bar, nor with group or cluster membership. Within some of the individual galaxies, we however observe significant differences in  $\langle SFR_5 \rangle / \langle SFR_{200} \rangle$  between the arm and interarm regions. In half of the galaxies, the recent SFH of both arm and interarm regions has been very similar. However, in the galaxies with higher bulge-to-total light ratios and earlier morphological type, the SFR is declining more rapidly in the interarm regions. This decline in SFR is not a result of low molecular gas surface density or a decrease in the star formation efficiency, implying that other factors are responsible for this SFR decrease.

**Key words:** galaxies: spiral – galaxies: star formation – galaxies: evolution

## 1 INTRODUCTION

Star formation (SF) changes in galaxies can occur both on global and local physical scales over a variety of time periods. Global and long-term changes are responsible for the blue and red sequence of galaxies illustrated by the bimodal distribution of galaxies in the colour-magnitude diagram or the star-forming main sequence (SFMS) (e.g. [Noeske et al. 2007](#); [Wuyts et al. 2011](#); [van der Wel et al. 2014](#)). Non-permanent as well as local changes inside a galaxy are responsible for the oscillations and scatter around the SFMS (e.g. [Tacchella et al. 2016](#)).

A galaxy’s ability to form stars is constrained by the availability of cold and dense gas, with a range of processes that can affect gas reservoirs and their efficiency at forming stars. In rich galaxy environments, such as groups and clusters, a galaxy can become significantly depleted of gas through ram-pressure stripping (e.g., [Gunn & Gott 1972](#); [Abadi et al. 1999](#); [Quilis et al. 2000](#); [Boselli et al. 2022](#)) or strangulation, when further gas accretion is inhibited by the removal, heating or stabilisation of the gaseous envelope around a galaxy ([Larson 1974](#); [Balogh et al. 2000](#); [Balogh & Morris 2000](#); [Kereš et al. 2005](#); [Dekel & Birnboim 2006](#)). However, if a galaxy manages to resume gas accretion, its SF activity may become rejuvenated, even if it was previously terminated or heavily subdued ([Lemonias et al. 2011](#); [Fang et al. 2012](#)).

AGN activity has long been known to decrease or quench SF via AGN-driven outflows that remove gas from the galaxy and suppress the cold accretion (e.g., [Croton et al. 2006](#); [Heckman & Best 2014](#)).

However, if the power output of the AGN reduces, the SF can reignite gain. Moreover, AGN jets can conversely shock the gas and compress the ISM, creating cocoons of turbulent gas, where molecular hydrogen is able to clump more efficiently and form stars (e.g., [Silk & Nusser 2010](#)). In simulations, a subsequent increase in the SF can also occur further out in the disk due to the pressurised ISM ([Gaibler et al. 2012](#); [Ishibashi & Fabian 2012](#)). These opposing effects of AGN feedback on the SF might depend on the type and power of the jet ([Kalfountzou et al. 2017](#)) and can even co-exist inside a galaxy ([Shin et al. 2019](#); [Mercedes-Feliz et al. 2023](#)). Feedback from stellar winds generated by massive SF has a similar ability to blow out the gas from a galaxy, even in the local Universe ([Chen et al. 2010](#)).

Mergers can trigger the AGN as they are able to funnel gas towards the galactic centre which also leads to a central starburst ([Hernquist & Mihos 1995](#); [Sanders & Mirabel 1996](#); [Veilleux et al. 2002](#); [Hopkins et al. 2006](#); [Engel et al. 2010](#)). The SF boost is likely to be short-lived ( $\sim 100$  Myr) due to the depletion of the molecular gas and AGN feedback (e.g., [Di Matteo et al. 2005](#)). Minor mergers can also have an impact on star-forming spiral galaxies, leading to SF quenching and a change in the morphology (e.g., [Bekki 1998](#); [Aguerri et al. 2001](#)). Conversely, in some cases, gas-rich minor mergers, have been shown to reignite recent SF in otherwise quiescent early-type galaxies ([Kaviraj et al. 2009](#)).

As mentioned above, intense SF in the galactic centre leads to a build-up of a large central spheroidal component. The bulge not only alters the morphology of a galaxy, but can also affect further star formation by stabilising the gas disk against fragmentation, lowering the efficiency of the SF process (e.g., [Martig et al. 2009](#); [Ceverino et al. 2010](#); [Bundy et al. 2010](#); [Fang et al. 2013](#)).

\* E-mail: maria.lomaeva.19@ucl.ac.uk

Galactic bars also appear to have a dual effect on SF. Gas in barred galaxies can lose angular momentum via gravitational torques, flow inwards (e.g., Shlosman et al. 1990; Kim et al. 2011; Shin et al. 2017). An increased central molecular gas concentration in barred galaxies has also been confirmed observationally (e.g., Sakamoto et al. 1999; Sheth et al. 2005). Some bars lead to the formation of a circumnuclear gas ring (e.g., Colina et al. 1997). Given the abundance of gas, a higher SFR is also expected in the centre of barred galaxies (Alonso-Herrero & Knapen 2001; Hunt et al. 2008; Ellison et al. 2011; Wang et al. 2012; Catalán-Torrecilla et al. 2017; Chown et al. 2019; Zee et al. 2023); however, in some cases, the opposite is seen (Sheth et al. 2005; Wang et al. 2012, 2020). This discrepancy is likely a consequence of the evolution of the bar. An increased SF activity could be attributed to the early stages of the bar growth, when there is much cold gas present (Athanasoula et al. 2013), but ultimately becomes depleted (Newnham et al. 2020) or rendered too turbulent to collapse (Khoperskov et al. 2018), which leads to quenching. Moreover, bar-driven gas inflows can occur multiple times during the evolution of a galaxy (Jogee et al. 2005).

Spiral structure in a galaxy is known for its ability to increase gas density, which favours SF (e.g., Elmegreen & Elmegreen 1983; Elmegreen 1994; Kim et al. 2020). There has been an ongoing debate whether the spiral structure is also able to boost the star formation efficiency (SFE) (Vogel et al. 1988; Lord & Young 1990; Cepa & Beckman 1990; Knapen et al. 1996; Seigar & James 2002; Gao et al. 2021) or not (Foyle et al. 2010; Kreckel et al. 2016; Schinnerer et al. 2017; Querejeta et al. 2021). In addition, more tightly wound spiral arms are observed in redder, earlier type galaxies with higher stellar mass, and higher degree of central concentration (Yu & Ho 2020), and the spiral arms strength shows a positive correlation with SFR (Yu et al. 2021).

The complex interplay between the processes described above is recorded by the star formation histories (SFHs) of galaxies. A possible approach to gauge SFHs is via spectral energy distribution (SED) fitting. This method is, however, proven to be rather complicated as real SFHs are very diverse, requiring a great deal of high-quality data and various model assumptions (e.g., Papovich et al. 2001; Shapley et al. 2001; Muzzin et al. 2009; Conroy 2013; Ciesla et al. 2016, 2017; Carnall et al. 2019; Leja et al. 2019), with short-term ( $\sim 100$  Myr) variations being especially difficult to pinpoint (e.g., Ocvirk et al. 2006; Gallazzi & Bell 2009; Zibetti et al. 2009; Leja et al. 2019). A different approach that allows to study recent SFHs is done by comparing SF from the recent (5–10 Myr) and more distant (0.1–1 Gyr) past through observations (Sullivan et al. 2000; Wuyts et al. 2011; Weisz et al. 2012; Guo et al. 2016; Emami et al. 2019; Faisst et al. 2019; Wolf et al. 2019; Wang & Lilly 2020; Byun et al. 2021; Karachentsev et al. 2021) and simulations (Sparre et al. 2017; Broussard et al. 2019; Flores Velázquez et al. 2021) of galaxies.

A common practise in this case is to probe recent SFHs by comparing  $H\alpha$  line and far ultraviolet (FUV) continuum emission. Since the bulk of  $H\alpha$  emission originates from the recombination of hydrogen atoms ionised by young massive stars, it traces SF on timescales of  $\lesssim 5$ –10 Myr (the typical main sequence lifetime of the O and B stars capable of ionising the gas). FUV observations, on the other hand, probe longer timescales of  $\sim 100$ –200 Myr as the FUV radiation is emitted directly by young massive stars that have escaped their birth clouds (Kennicutt & Evans 2012).

In Lomaeva et al. (2022) (hereafter Paper I) we studied recent SFHs by calibrating a prescription that estimates the rate of change in the SFR at the present time,  $dSFR/dt$ . We aimed to use simple observables instead of full SED modeling of SFHs to avoid the strict data requirements and large computational costs associated

with that. Instead, we opted for a calibrated method that relies on as few observables as possible. This metric,  $\langle SFR_5 \rangle / \langle SFR_{200} \rangle$ , which is the ratio between the SFR averaged over the past 5 and 200 Myr as a function of the  $H\alpha$ –FUV colour, was calculated via a set of models generated in CIGALE (Code Investigating GALaxy Emission; Burgarella et al. 2005; Noll et al. 2009; Boquien et al. 2019).

In Paper I, we applied  $\langle SFR_5 \rangle / \langle SFR_{200} \rangle$  to a grand-design nearby spiral NGC 628 seen almost perfectly face-on (inclination of  $8.9^\circ$ ; Leroy et al. 2021b). In this work, we extend our sample to 11 galaxies, including NGC 628, based on the observations within the PHANGS (the Physics at High Angular resolution in Nearby Galaxies project)<sup>1</sup> ALMA (Leroy et al. 2021a,b) and MUSE (Emsellem et al. 2022) samples. The selected disk galaxies are star-forming, nearby ( $< 20$  Mpc), mostly face-on, with their optical images shown in the 1<sup>st</sup> column of Figure 1. They show a diversity of external (field vs. group/cluster) and internal (AGN vs. inactive; barred, unbarred, and disks without spirals) properties, which is perfect for examining recent changes in SFHs and potential physical processes behind them.

This paper is structured as follows: in Section 2 we describe the observational data required for the analysis. In Section 3, we briefly mention how the  $\langle SFR_5 \rangle / \langle SFR_{200} \rangle$  metric was defined in Paper I. In Section 4, we present the results showing  $\langle SFR_5 \rangle / \langle SFR_{200} \rangle$  differences between the eleven galaxies sampled, the SFE behaviour within different internal galactic environments, and the difference in the distribution of  $\langle SFR_5 \rangle / \langle SFR_{200} \rangle$  in the interarms vs. arms of some of the galaxies. Finally, in Section 5, we discuss potential physical and artificial causes of the  $\langle SFR_5 \rangle / \langle SFR_{200} \rangle$  differences in the arms-interarms as well as conclude the main findings in Section 6.

## 2 OBSERVATIONS

### 2.1 Photometry

Our analysis required photometric observations in three bands: far-UV (FUV), near- and mid-infrared (NIR and MIR, respectively). The FUV observations are required as an input for the  $\langle SFR_5 \rangle / \langle SFR_{200} \rangle$  diagnostic, while the NIR and MIR data are used for correcting the FUV images for dust attenuation as well as for masking pixels with no recent SF (see Section 2.2). For those, we selected FUV images obtained by the GALaxy Evolution eXplorer (GALEX; Martin et al. 2005; Morrissey et al. 2007), J-band images from the 2 Micron All-Sky Survey (2MASS; Skrutskie et al. 2006), as well as  $3.6\mu\text{m}$  and  $24\mu\text{m}$  images collected with the InfraRed Array Camera (IRAC; Fazio et al. 2004) and the Multiband Imager (MIPS; Rieke et al. 2004) on-board *Spitzer* (Werner et al. 2004). The final sample selection in this work was dependent on the availability of the photometric data in these three bands among the PHANGS-MUSE galaxies, which left us with 11 objects.

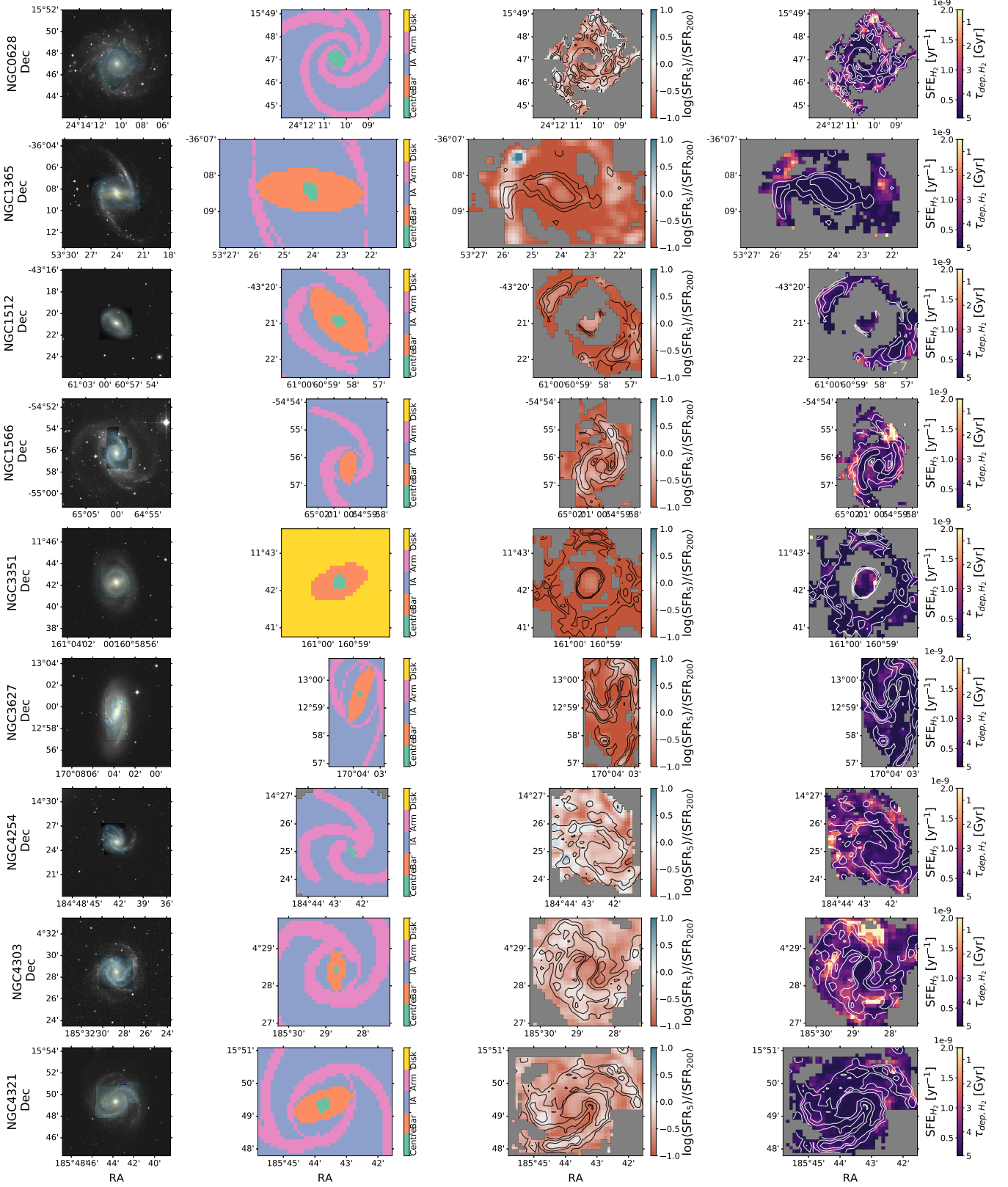
We downloaded the images from the DustPedia Archive<sup>2</sup> as well as the NED archive<sup>3</sup>. The DustPedia sample contains matched aperture photometric images of 875 nearby galaxies in over 40 bands.

We also performed a check to estimate the sky background and removed it whenever applicable. We removed the foreground stars following the procedure in Paper I. Briefly, we identified the stars using the SIMBAD database (Wenger et al. 2000) and fitted a 2D

<sup>1</sup> <https://sites.google.com/view/phangs/home/data>

<sup>2</sup> <http://dustpedia.astro.noa.gr>

<sup>3</sup> <http://ned.ipac.caltech.edu>



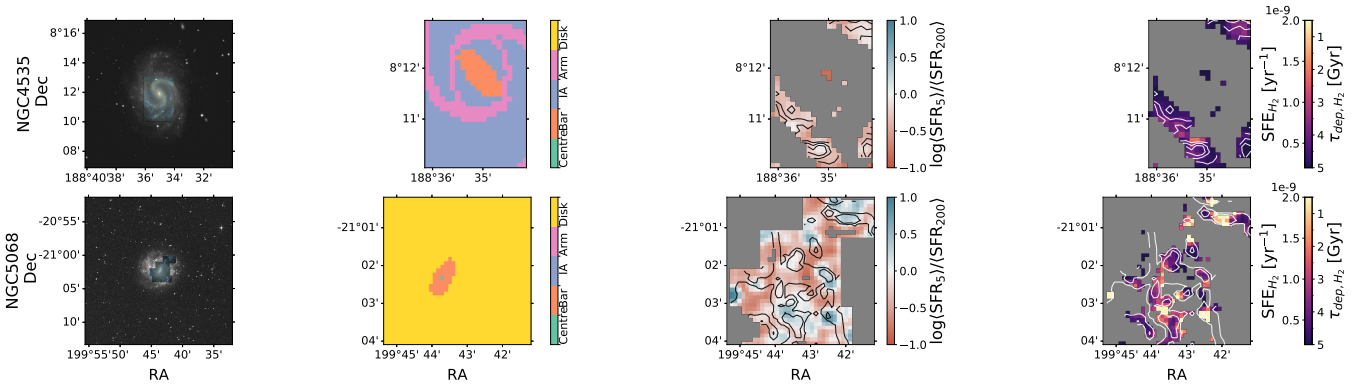


**Figure 1.** The eleven galaxies observed. *First column from the left:* an  $R$ -band DSS image overlaid with a  $gri$ -band photometric image from the PHANGS-MUSE sample (Emsellem et al. 2022) to illustrate the region considered in this work. *Second column:* the environmental mask from Querejeta et al. (2021) convolved and rebinned to the  $6''$  resolution and pixel size showing the central region, galactic bar, interarms, spiral arms, and disk without spirals if applicable. *Third column:* the  $\log\langle SFR_5 \rangle / \langle SFR_{200} \rangle$  metric with the contours showing the  $\Sigma_{\text{mol}}$  concentration above the typical noise level. *Fourth column:* molecular SFE with the same contours as in the third column. The left-hand side of the colour bar shows SFE in the units of  $\text{yr}^{-1}$ , while the right-hand side exhibits the corresponding depletion time,  $\tau_{\text{mol}}$  in Gyr.

Moffat profile to each star with the MPDAF package (Bacon et al. 2016; Piqueras et al. 2019) in PYTHON. With the FWHM of the Moffat profile, we centred a circular annulus and aperture at each star with the PHOTUTILS (Bradley et al. 2020) package in PYTHON and replaced the pixels inside the aperture with random numbers generated knowing the mean and one standard deviation of the immediately adjacent and sigma-clipped pixels inside the annulus. The sigma clipping was done using ASTROPY (Astropy Collaboration et al. 2013, 2018) with a  $2\sigma$  threshold. The MIPS  $24\mu\text{m}$  data has the lowest resolution of  $6''$ , hence, all other data products were convolved to this resolution. That is a slight improvement in resolution compared to Paper I where all observations were convolved to  $7''$ .

The photometric observations were corrected for the Galactic extinction using the Cardelli et al. (1989) dust extinction law with  $E(B - V)$  values from Schlafly & Finkbeiner (2011), assuming the Galactic total-to-selective extinction value of  $R_V = 3.1$ .

The intrinsic UV luminosity emitted by the source,  $L(UV)_{\text{int}}$ , is partly absorbed and re-emitted by the dust at infrared wavelengths. A common method to account for this effect is formulated by:

$$L(UV)_{\text{int}} = L(UV)_{\text{obs}} + k \times L(IR), \quad (1)$$

where  $L(UV)_{\text{obs}}$  is the observed luminosity,  $k$  is the scaling coefficient, and  $L(IR)$  is the observed IR luminosity in the corresponding band. Leroy et al. (2019) derived a value for  $k = 4.9$  using GALEX and Wide-field Infrared Survey Explorer (WISE) observations at  $22\mu\text{m}$  and SED fitting from Salim et al. (2016, 2018), which we employ in this work. This value was calibrated for a resolved sample of  $\sim 15\,750$  nearby galaxies.

However, in Paper I, we corrected the FUV images for dust extinction following the recipe from Boquien et al. (2016) instead. Briefly, Boquien et al. (2016) performed a spatially resolved, multi-wavelength study of eight star-forming spiral galaxies from the KINGFISH survey (Kennicutt et al. 2011). Through SED fitting, the authors derived an equation connecting the  $k$  coefficient and several photometric colours to estimate the variable impact of dust heated by old stellar populations (see their Table 4). The dust attenuation curves retrieved from numerical SED modelling tend to be steeper than the starburst curve inferred from empirical methods (e.g., Calzetti et al. 1994, 2000). In our case, a curve that is significantly steeper than the star-burst Calzetti et al. (2000) curve that we use to correct the  $H\alpha$  emission for dust attenuation in Section 2.2, could add a systematic

discrepancy. The recommendation of Leroy et al. (2019) has also been used in other recent studies (e.g., Belfiore et al. 2023), which makes it easier to compare our results with the recent literature. We further discuss these effects on our results in Section 5.2.1. For consistency, we explore the impact of both FUV attenuation methods using MIPS  $24\mu\text{m}$  observations. For  $k$  derived as in Boquien et al. (2016) we used:

$$k = 15.044 - 2.169 \times (\text{FUV-IRAC } 3.6), \quad (2)$$

setting  $L(IR) = L(\text{MIPS } 24\mu\text{m})$  as listed as a possible IR band option in Boquien et al. (2016).

## 2.2 Optical observations

We used integrated line emission maps of the  $H\alpha$ ,  $H\beta$ ,  $[\text{O III}]\lambda 5006 \text{ \AA}$ , and the  $[\text{Si II}]\lambda 6716, 6731 \text{ \AA}$  doublet emission obtained with the MUSE spectrograph (the Multi Unit Spectroscopic Explorer; Bacon et al. 2010) at the Very Large Telescope (VLT). These observations were part of the PHANGS-MUSE survey (Emsellem et al. 2022). In total, the PHANGS-MUSE survey contains maps of 19 massive ( $9.4 < \log(M_\star/M_\odot) < 11.0$ ) nearby ( $D \lesssim 20 \text{ Mpc}$ ) star-forming disc galaxies. There are 168 MUSE pointings ( $1'$  by  $1'$  each) with typical seeing ranges from  $0.7$ - $1''$ . Rather than using the data products at the native MUSE resolution, we opted for the data convolved and optimised (*copt*), that is their point spread function (PSF) was set to be a circular two-dimensional Gaussian with a FWHM that is constant as a function of wavelength and position within each mosaic. Those data products were subsequently convolved to  $6''$  resolution to match the photometry. We applied a signal-to-noise (S/N) ratio cut of 5 to all optical observations.

Emsellem et al. (2022) subtracted the sky background and corrected the MUSE data for foreground Galactic extinction using the O'Donnell (1994) extinction curve and the  $E(B - V)$  values from Schlafly & Finkbeiner (2011). Since the O'Donnell (1994) extinction curve is only defined down to near-UV (NUV) wavelengths, we used the Cardelli et al. (1989) curve instead that is available in the FUV for consistency. We also used the Galactic total-to-selective extinction value of  $R_V = 3.1$ . The foreground stars were removed following the procedure described in Section 2.1.

Working with timescales as short as 5 Myr, that is with environments where dust and gas are mixed together, we needed to account

for dust attenuation of the  $H\alpha$  emission,  $A(H\alpha)$ . We calculated it for each spaxel from the Balmer decrement,  $F(H\alpha)/F(H\beta)$  assuming Case B recombination (Osterbrock & Ferland 2006):

$$A(H\alpha) [\text{mag}] = \frac{E(H\beta - H\alpha)}{k(H\beta) - k(H\alpha)} \cdot k(H\alpha) = \frac{2.5 \log \left( \frac{1}{2.86} \cdot \frac{F(H\alpha)}{F(H\beta)} \right)}{\frac{k(H\beta)}{k(H\alpha)} - 1}, \quad (3)$$

where  $\frac{k(H\beta)}{k(H\alpha)}$  is the reddening curve ratio of 1.53 for the Calzetti et al. (2000) curve assuming  $R_V = 3.1$  (Cardelli et al. 1989).

From this, we obtained the attenuation-corrected luminosity:

$$L(H\alpha)_{\text{corr}} = L(H\alpha)_{\text{obs}} \times 10^{0.4A(H\alpha)}, \quad (4)$$

where  $L(H\alpha)_{\text{obs}}$  is the observed, attenuated  $H\alpha$  luminosity.

Finally, we were able to calculate the SFR from the  $H\alpha$  line emission assuming a Kroupa (2001) initial mass function (IMF), as described in Calzetti (2013):

$$\text{SFR} [M_{\odot} \text{ yr}^{-1}] = 5.5 \times 10^{-42} \times L(H\alpha)_{\text{corr}}, \quad (5)$$

where  $L(H\alpha)_{\text{corr}}$  is in units of  $\text{erg s}^{-1}$ .

### 2.3 PHANGS-ALMA

In addition to the optical observations, we also obtained  $^{12}\text{CO}(J=2 \rightarrow 1)$  line emission, hereafter CO(2-1), from the PHANGS-ALMA survey (PI: E. Schinnerer; Leroy et al. 2021a,b). Limited by the MIPS  $24\mu\text{m}$  resolution, we used the line-integrated CO(2-1) intensity observations (broad mom0 map) at  $7.5''$  resolution and a  $1\sigma$  sensitivity of  $5.5 \text{ mJy beam}^{-1}$  per  $2.54 \text{ km s}^{-1}$  channel. We applied an S/N ratio cut of 3 to the ALMA data.

To calculate the molecular gas mass surface density,  $\Sigma_{\text{mol}}$ , from the line-integrated CO(2-1) intensity,  $I_{\text{CO}(2-1)}$ , in  $\text{K km s}^{-1}$ , we used the relation:

$$\Sigma_{\text{mol}} [M_{\odot} \text{ pc}^{-2}] = \alpha_{\text{CO}}^{1-0} \cdot R_{21}^{-1} \cdot I_{\text{CO}(2-1)} \cdot \cos i, \quad (6)$$

where  $\alpha_{\text{CO}}^{1-0}$  is the CO(1-0) conversion factor in  $M_{\odot} \text{ pc}^{-2} (\text{K km s}^{-1})^{-1}$ ,  $R_{21}$  is the CO(2-1)-to-CO(1-0) line ratio, and  $i$  is the inclination. We assumed  $R_{21}=0.65$ , which is the non-weighted mean derived in den Brok et al. (2021), and adopted a constant Galactic value for  $\alpha_{\text{CO}}^{1-0}$  of  $4.35 M_{\odot} \text{ pc}^{-2} (\text{K km s}^{-1})^{-1}$ , as in Bolatto et al. (2013).

## 3 METHOD

### 3.1 $\langle SFR_5 \rangle / \langle SFR_{200} \rangle$ diagnostic

In Paper I, we defined and calibrated an SFR change diagnostic,  $\langle SFR_5 \rangle / \langle SFR_{200} \rangle$ , that allows to probe recent SFHs on timescales of 5–200 Myr and measure whether the SF has been increasing or decreasing in a given region inside a galaxy. The main advantage of this method is that it is based on simple observables instead of a full SED modeling. We tested this method on a well-known galaxy NGC 628, which is also included into the current study, with the purpose of applying this technique to a larger sample of star-forming galaxies in this work.

In summary, the diagnostic is based on the  $H\alpha$ –FUV colour which is used as an input to calculate the ratio between the SFR averaged over the past 5 and 200 Myr. We used synthetic models generated with CIGALE (Code Investigating GALaxy Emission; Burgarella

et al. 2005; Noll et al. 2009; Boquien et al. 2019) to calibrate the metric and gauge potential degeneracies between  $H\alpha$ –FUV colour and different SFHs (see Paper I).

We calculated the  $H\alpha$ –FUV colour as:

$$H\alpha\text{--FUV} = -2.5 \cdot \log(\text{LyC} [\text{mJy}]) + 20 - \text{FUV} [\text{mag}], \quad (7)$$

where  $\log \text{LyC}$  is the Lyman continuum photons flux density that ionise  $\text{H II}$  regions derived from the  $H\alpha$  luminosity, as presented and used in Boselli et al. (2016, 2018a, 2021). For our sample, the median uncertainty in the  $H\alpha$ –FUV colour remains within 10% for all galaxies.

In the next step, we generated a set of models in CIGALE that would represent hypothetical galaxies with varying levels of their recent SF. Briefly, we assumed a Chabrier (2003) IMF and stellar population synthesis models for the stellar emission from Bruzual & Charlot (2003). For the parametric SFH, we chose a delayed SFH with a constant instantaneous increase or drop in the SFR ( $\text{SFH}_{\text{DELAYEDBQ}}$ ). Using the results from Declair et al. (2019), who carried out SED fitting to individual pixels in NGC 628, we set the range of SFH parameters, such as the age,  $A_{\text{main}}$ , and the e-folding time,  $\tau_{\text{main}}$ , of the main stellar populations. The strength of the SFR increase/decrease was parameterised by  $r_{\text{SFR}}$ , that is the ratio between the SFR after and before this event. As a result,  $r_{\text{SFR}} < 1$  represents a suppression in recent SF,  $r_{\text{SFR}} > 1$  denotes an increase in SF, and  $r_{\text{SFR}} = 1$  gives no change in the SFR. The lookback time in Myr of this SF boost/drop was set by  $A_{\text{bq}}$ . Finally, we assumed a dust-free scenario in CIGALE and instead corrected the observed  $H\alpha$ –FUV colour for attenuation effects. All parameter ranges and a more detailed discussion on this procedure are presented in Paper I (Section 3).

From the CIGALE models, we obtained a trend for  $\langle SFR_5 \rangle / \langle SFR_{200} \rangle$  as a function of the  $H\alpha$ –FUV colour and fitted a curve to this trend using the LMFIT package in PYTHON. This yielded:

$$\langle SFR_5 \rangle / \langle SFR_{200} \rangle_{\text{fit}} = \exp[-10.123 \cdot \arctan(0.456 \cdot (H\alpha - \text{FUV})) + 0.244 \cdot (H\alpha - \text{FUV}) + 7.820]. \quad (8)$$

In Paper I, we discussed two cases where the CIGALE models deviated from the main trend described by Equation 8. In the first case, we saw a set of models where SF was quenched very strongly and abruptly, with  $r_{\text{SFR}} < 0.001$ . We deem such scenarios unlikely in real galaxies. In the second case, recent changes in the SF activity could not be efficiently probed by the  $\langle SFR_5 \rangle / \langle SFR_{200} \rangle$  parameter when no recent SF formation has occurred. To eliminate this quiescent scenario, we applied two additional constraints. The first one eliminates pixels that are too red in the FUV–IRAC  $3.6\mu\text{m}$  colour ( $> 3 \text{ mag}$ ), while the second one removes the regions where  $H\alpha$  emission does not originate from SF, that is, the equivalent width of the  $H\alpha$  line,  $\text{EW}(H\alpha)$ , is too small ( $< 5 \text{ \AA}$ ). Since  $\text{EW}(H\alpha)$  observations were not available among the PHANGS-MUSE data products, we selected a different criterion, the NUV–J colour, such that  $\text{NUV–J} > 3.75 \text{ mag}$  were masked out due to no recent SF.

## 4 RECENT CHANGES IN THE STAR FORMATION ACTIVITY

The distributions of  $\langle SFR_5 \rangle / \langle SFR_{200} \rangle$  in each galaxy shown in Figure 2 tend to create two groups of galaxies peaking at higher (H) and lower (L) values of  $\langle SFR_5 \rangle / \langle SFR_{200} \rangle$ . NGC 628, 4254, 4303, 4321, 4535, and 5068 belong to the high end of the  $\langle SFR_5 \rangle / \langle SFR_{200} \rangle$  distribution, while NGC 1365, 1512, 1566, 3351, and 3627 belong to its low end. This is also summarised in the last column of Table 2.

**Table 1.** The eleven galaxies studied in this work and some of their properties.

Name	Type	RA [hms]	Dec [dms]	$D^a$ [Mpc]	$i^b$ [deg]	$\log M_\star^c$ [ $M_\odot$ ]	$\log SFR^c$ [ $M_\odot \text{ yr}^{-1}$ ]	$12+\log(\text{O}/\text{H})^d$ [dex]	Pixel scale <sup>e</sup> [pc pixel <sup>-1</sup> ]
NGC 628	Sc	01h36m41.75s	+15d47m01.1s	9.8	8.9	10.34	0.24	8.48	285.1
NGC 1365	Sb	03h33m36.46s	-36d08m26.4s	19.6	55.4	10.99	1.23	8.48	570.1
NGC 1512	Sa	04h03m54.28s	-43d20m55.9s	18.8	42.5	10.71	0.11	8.57	546.9
NGC 1566	SABb	04h20m00.40s	-54d56m16.6s	17.7	29.5	10.78	0.66	8.58	514.9
NGC 3351	Sb	10h43m57.73s	+11d42m13.3s	10.0	45.1	10.36	0.12	8.59	290.9
NGC 3627	Sb	11h20m15.03s	+12d59m28.6s	11.3	57.3	10.83	0.58	8.54	328.7
NGC 4254	Sc	12h18m49.63s	+14d24m59.4s	13.1	34.4	10.42	0.49	8.56	381.1
NGC 4303	Sbc	12h21m54.93s	+04d28m25.6s	17.0	23.5	10.52	0.73	8.58	494.5
NGC 4321	SABb	12h22m54.93s	+15d49m20.3s	15.2	38.5	10.75	0.55	8.56	442.1
NGC 4535	Sc	12h34m20.34s	+08d11m51.9s	15.8	44.7	10.53	0.33	8.54	459.6
NGC 5068	Sc	13h18m54.81s	-21d02m20.8s	5.2	35.7	9.40	-0.56	8.32	151.3

<sup>a</sup> Anand et al. (2021)<sup>b</sup> Lang et al. (2020)<sup>c</sup> Leroy et al. (2021a)<sup>d</sup> At  $r_{\text{eff}}$  from Groves et al. (2023)<sup>e</sup> Rebinned to 6'' per pixel

Looking at the  $\langle SFR_5 \rangle / \langle SFR_{200} \rangle$  distribution across the galactic disks in the 3<sup>rd</sup> column of Figure 1, we observe large areas of increasing recent SF in NGC 628, 4254, 4303, and 4321, while NGC 1512, 1566, and 3627 exhibit recent SF activity that ranges from roughly unchanged to decreasing. The most active galaxy in terms of recent SF changes is the low-mass galaxy NGC 5068. NGC 1365 shows a region with a very strong recent SF increase, visually similar to the headlight cloud in NGC 628 (Herrera et al. 2020). NGC 3351 is the only galaxy in the sample that has a consistently decreasing recent SF across the entire disk observed. Finally, NGC 4535 shows a slight increase in the recent SF in the arm regions, although a large fraction of the observed pixels is masked out due to the limitations of the  $H\beta$  line SNR.

#### 4.1 The impact of AGN, bars, and external effects on recent SF

In this section, we examine if there is any connection between a galaxy's position in the  $\langle SFR_5 \rangle / \langle SFR_{200} \rangle$  distributions, AGN, galactic bar, vicinity to other galaxies, and past gravitational interactions with other group/cluster members. We summarise these properties in Table 2.

##### 4.1.1 AGN feedback

Among AGN hosts in the sample, there are Seyfert galaxies NGC 1365 (Véron-Cetty & Véron 2006) and NGC 1566 (Shobbrook 1966), low ionization nuclear emission region (LINER)/Seyfert type 2 galaxies NGC 4303 and NGC 3627 (Ho et al. 1997), and the starburst NGC 4321 which is another LINER galaxy (Wozniak et al. 1999).

For NGC 1365, Gao et al. (2021) showed that the feedback from the AGN or hot shocked gas can push away molecular and atomic hydrogen gas at a speed up to  $100 \text{ km s}^{-1}$ . They saw that the outflow of the molecular gas is faster than the SF, suggesting a negative feedback scenario.  $\langle SFR_5 \rangle / \langle SFR_{200} \rangle$  indicates a drop in the SF activity in the central region of NGC 1365, in agreement with this statement.

In NGC 1566, the super-massive black hole influences the gas dynamics reverting the gravity torques, as shown in Combes et al. (2014). This drives the gas inwards and possibly fuels the AGN.

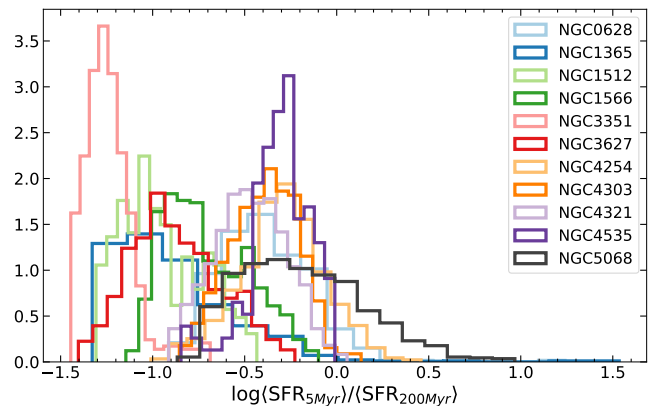


**Figure 2.** The distribution of  $\log \langle SFR_5 \rangle / \langle SFR_{200} \rangle$  in the observed galaxies, as defined in Equation 8. This shows that galaxies create two groups peaking at lower and higher values of  $\langle SFR_5 \rangle / \langle SFR_{200} \rangle$ , as summarised in the last column in Table 2. The histograms were normalised to have the same area of unity.

Galaxies with no confirmed or debated AGN include NGC 628 (Liu et al. 2005; Alston et al. 2021), NGC 1512 (Ducci et al. 2014), NGC 3351 (Gadotti et al. 2019), NGC 4254 (Burtcher et al. 2021), NGC 4535<sup>4</sup>, and NGC 5068<sup>5</sup>.

We also note that it is likely that the presence of an AGN would not have a substantial effect on the SF activity, unless the AGN duty cycle is much longer than typically assumed. This is a result of the large differences between the dynamical timescales of the AGN and the galaxy as a whole.

##### 4.1.2 Galactic bar presence

There are nine galaxies in the sample that have a galactic bar, as per the environmental masks in Querejeta et al. (2021): NGC 1365, 1512, 1566, 3351, 3627, 4303, 4321, 4535, and 5068, while NGC 628 and NGC 4254 have no bar.

<sup>4</sup> As per NED <https://ned.ipac.caltech.edu/>

<sup>5</sup> See Footnote 4

**Table 2.** The summary of the internal and external properties of the eleven galaxies studied in this work. References for the columns AGN, Field, and Interacting can be found in Section 4.1. The  $\langle SFR_5 \rangle / \langle SFR_{200} \rangle$  column denotes if a galaxy belongs to the high (H) or low (L) end of the  $\langle SFR_5 \rangle / \langle SFR_{200} \rangle$  distribution in Figure 2.

Name	AGN [Yes/No]	Bar [Yes/No]	Field [Yes/No]	Interacting [Yes/No]	$\langle SFR_5 \rangle / \langle SFR_{200} \rangle$ [Low/High]
NGC 628	N	N	N	N	H
NGC 1365	Y	Y	N	N	L
NGC 1512	N	Y	N	Y	L
NGC 1566	Y	Y	N	Y	L
NGC 3351	N	Y	Y	N	L
NGC 3627	Y	Y	N	Y	L
NGC 4254	N	N	N	Y	H
NGC 4303	Y	Y	N	N	H
NGC 4321	Y	Y	N	N	H
NGC 4535	N	Y	N	N	H
NGC 5068	N	Y	Y	N	H

NGC 1365 is dubbed the Great Barred Spiral Galaxy and has the highest global SFR and stellar mass in our sample, with most of the SF occurring in the central starburst ring. Schinnerer et al. (2023) found that the large-scale stellar bar in NGC 1365 drives gas inwards and might be solely responsible for the massive SF in the central 5 kpc, without any significant AGN feedback on the gas disk.

NGC 1512 has a double ring structure with one ring located around the nucleus and another one situated in the disk, which is not uncommon in barred galaxies. Ma et al. (2017, 2018) estimated the age of the nuclear ring in NGC 1512 to be  $\sim 40$  Myr on average. The  $\langle SFR_5 \rangle / \langle SFR_{200} \rangle$  metric indicates a moderate decline in the recent SF activity in the central part of the galaxy, in line with these findings. NGC 1566 also has a double ring structure, where the rings are formed by the wound-up spiral arms. NGC 3351 contains a circumnuclear ring as well with intense massive SF (e.g., Alloin & Nieto 1982; Colina et al. 1997) and an inner ring at a larger radius. Previous studies have revealed the gas and dust in the circumnuclear ring are accumulated via the bar (e.g., Leaman et al. 2019).

Iles et al. (2022) simulated interacting and isolated bars to match NGC 3627 and NGC 4303, respectively. They found that the presence of a bar boosts SF activity in both cases, however, occurring gravitational interactions cause an additional burst-like period of the SF, likely due to the consolidation of the spiral arm before the bar forms. Indeed, we see that  $\langle SFR_5 \rangle / \langle SFR_{200} \rangle$  decreases more in NGC 3627 than in NGC 4303, which could be due to a stronger gas depletion in NGC 3627 during the earlier SF bursts.

#### 4.1.3 Cluster/group membership

There are two galaxies in the sample that are isolated field galaxies: NGC 3351 (Young et al. 1996) and NGC 5068 (Karachentsev et al. 2002).

Among the galaxies that belong either to a group or a cluster, there are NGC 628, 1365, 1512, 1566, 3627, 4303, 4254, 4321, and 4535.

NGC 628 is a member of the NGC 628 group (Garcia 1993). NGC 1365 is situated in the Fornax cluster (Lindblad 1999), while NGC 4303, 4254, 4321, and 4535 are located in the Virgo Cluster (Binggeli et al. 1985; Fouque et al. 1992). NGC 1512 and NGC 1566 are members of the Dorado group (Maia et al. 1989). Finally, NGC 3627 is a galaxy in the Leo Triplet (Ferrarese et al. 2000).

We caution, however, that a more thorough examination of the

group and cluster membership would require a consideration about its size or density as well as a galaxy’s position in it.

#### 4.1.4 Past gravitational interactions

Among interacting galaxies, there is NGC 1512, which is interacting with the dwarf galaxy NGC 1510. This galaxy pair is separated only by  $\sim 5'$  (13.8 kpc) (Koribalski & López-Sánchez 2009). NGC 1566 is also known to interact with its smaller companions (Kilborn et al. 2005). NGC 3627 has potentially interacted with the neighbouring NGC 3623 and NGC 3628 in the past (Haynes et al. 1979). NGC 4254 is likely to have experienced a rapid gravitational encounter with another cluster member 280–750 Myr ago (Vollmer et al. 2005; Boselli et al. 2018b). NGC 4321 has probably interacted with other cluster companions in the past as well (e.g., Knapen et al. 1993).

The non-interacting galaxies include NGC 628, 1365, 3351, 4303, 4321, 4535, and 5068. NGC 628 is considered isolated since it has not experienced any gravitational interactions in the past 1 Gyr (Kamphuis & Briggs 1992). This view has, however, been recently challenged (Weżgowiec et al. 2022). NGC 4535 is rather unperturbed, however, might be interacting with the cluster environment, potentially experiencing ram pressure stripping (Weżgowiec et al. 2007).

Overall, we see that the recent changes in the SF are difficult to pinpoint to the extragalactic environment, past and current gravitational interactions with other galaxies as well as the presence of an AGN and a galactic bar. We also bear in mind the low sample size in this study.

## 4.2 Effects of the internal galaxy environment on SFE

Similarly as in Paper I, we constructed a resolved Kennicutt-Schmidt relation, as shown in Figure 3. In the left panel of Figure 3, we see a gradient in  $\langle SFR_5 \rangle / \langle SFR_{200} \rangle$  for fixed  $\Sigma_{\text{mol}}$ . This gradient is somewhat steeper compared to the one of NGC 628 in Paper I since we chose a different method to correct for the FUV attenuation. A number of pixels with  $\log \langle SFR_5 \rangle / \langle SFR_{200} \rangle > 0$  are positioned at an intermediate value of  $\log \Sigma_{\text{mol}} \approx 0.9 M_{\odot} \text{ pc}^{-2}$  that belong to the low stellar mass galaxy NGC 5068. Low-mass galaxies do tend to experience a “burstier” SF (e.g., Weisz et al. 2012; Emami et al. 2019; Flores Velázquez et al. 2021), which, however, does not explain the high  $\langle SFR_5 \rangle / \langle SFR_{200} \rangle$  and SFE at the intermediate  $\log \Sigma_{\text{mol}}$ . Instead, we might actually underestimate  $\log \Sigma_{\text{mol}}$  in NGC 5068: having lower gas phase metallicity,  $A(\text{FUV})$ , and  $A(\text{H}\alpha)$  than the

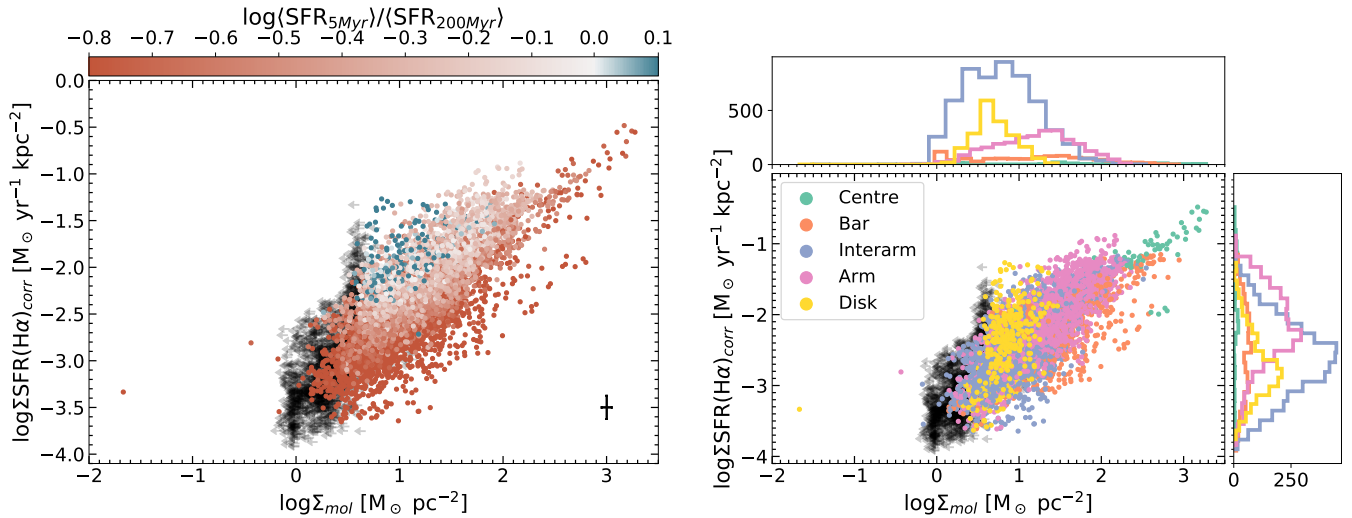


**Figure 3.** The resolved Kennicutt-Schmidt relation (rKS) of the galaxies sampled. The black arrows denote upper limits. *Left panel:* the rKS coloured by the  $\langle SFR_5 \rangle / \langle SFR_{200} \rangle$  metric, with blue and red data points indicating increased vs. decreased recent SF activity, respectively. The error bar represents the mean uncertainty among the galaxies for detected regions above the S/N cut. *Right panel:* the rKS coloured according to the different internal galactic environments taken from Querejeta et al. (2021). The top and right-most histograms show the respective distributions of  $\Sigma_{\text{mol}}$  and  $\Sigma_{\text{SFR}(\text{H}\alpha)}$  in the internal environments considered.

other galaxies in the sample, the assumption of a constant Galactic  $\alpha_{\text{CO}} = 4.35 \text{ M}_{\odot} \text{ pc}^{-2} (\text{K km s}^{-1})^{-1}$  is likely to be too low. It is known that CO molecules can become UV photo-dissociated in galaxies with a lower metal and dust content, while the  $\text{H}_2$  reservoir remains self-shielded (e.g., Amorín et al. 2016; Madden et al. 2020). A higher  $\alpha_{\text{CO}}$  would push the blue data points associated with NGC 5068 to higher  $\log \Sigma_{\text{mol}}$  values in Figure 3, rendering them more aligned with the overall trend. For example, the gas phase metallicity of  $Z = 8.32^6$  in NGC 5068 yields  $\alpha_{\text{CO}} = 17.7$ , following the recipe from Accurso et al. (2017). We do not opt for any variable  $\alpha_{\text{CO}}$  calibration here since it would introduce additional scatter to the analysis, while the correct approach to calculate  $\alpha_{\text{CO}}$  would also consider its radial variations, which is beyond the scope of this work.

One of the exercises of this work was to examine how different morphological structures inside a galaxy affect the SF. To separate each galaxy into the bulge, bar, arm and interarm regions, or alternatively disks without spirals, we applied a simple environmental mask from Querejeta et al. (2021)<sup>7</sup>. These masks were constructed from *Spitzer* IRAC  $3.6 \mu\text{m}$  images at  $\sim 1.7''$  resolution and later convolved and rebinned to  $6''$  resolution and pixel size to match the other observations.

Looking at the right-hand panel in Figure 3, we see that the interarm regions tend to have lower  $\log \Sigma_{\text{mol}}$  and  $\log \Sigma_{\text{SFR}(\text{H}\alpha)}$  compared to the arm regions. These results are in line with expectations that spiral arms tend to concentrate molecular gas which also increases the SFR (e.g., Kim et al. 2020) compared to the interarms. Galaxies, such as NGC 3351 and NGC 5068 that are classified as disk galaxies without spirals, show a similar SFR and molecular gas surface density distribution in the disk as the interarms regions in galaxies that do exhibit a spiral structure. The bars and galactic centres have overall a wide distribution of  $\log \Sigma_{\text{mol}}$  and  $\log \Sigma_{\text{SFR}(\text{H}\alpha)}$ , with the central pixels reaching out to the highest values of these quantities. These pixels are attributed to a single galaxy, NGC 1365. This galaxy is known for

its intense SF inside the central ring-like structure which is formed by the gas inflows driven by the large-scale stellar bar (Schinnerer et al. 2023). Galactic bars and bulges can have varying effects on the SFR and SFE due to complex gas dynamics (e.g., Querejeta et al. 2021; Iles et al. 2022; Maeda et al. 2023), hence the large spread of these pixels.

We also illustrate molecular SFEs ( $\text{SFE}_{\text{H}_2} = \Sigma_{\text{SFR}(\text{H}\alpha)} / \Sigma_{\text{mol}}$ ) in different internal environments in the rightmost panel of Figure 4 by plotting their distributions of the molecular SFE. We are also interested if these trends are affected by  $\text{H}\alpha$  emission unrelated to the SF, such as the emission from the diffuse ionised gas (DIG). The DIG contribution is especially important in the interarm region where the SF is generally low. To identify such pixels we constructed a Baldwin, Phillips, Terlevich (BPT; Baldwin et al. 1981) diagram with the extreme starburst classification line computed by Kewley et al. (2001) and the Seyfert and low-ionization narrow emission-line (LINER) separation from Kewley et al. (2006).

The arm-interarm regions peak at somewhat higher SFE values compared to the bulges, bars, and disks without spirals. The removal of the DIG pixels does not change the SFE distribution in the interarms, similarly as for  $\langle SFR_5 \rangle / \langle SFR_{200} \rangle$ , as mentioned further in Section 4.3. Nevertheless, the Kolmogorov-Smirnov test (K-S test) yielded a statistically significant p-value, meaning that the arm and interarm samples of the SFE are intrinsically different. This actually disagrees with the corresponding results for NGC 628 in Paper I, where we found that the SFE in the arms and interarms was similarly distributed.

There have been a number of studies examining whether the SFE in the galactic bars and disks are different. Some works have seen a suppression of the SFE in bars despite available molecular gas (Momose et al. 2010; Maeda et al. 2020, 2023), while other works have not observed any such SFE suppression (Saintonge et al. 2012; Díaz-García et al. 2021; Querejeta et al. 2021; Muraoka et al. 2019). In our sample, we find that the  $\text{SFE}_{\text{bar}} / \text{SFE}_{\text{arm}} = 0.44$ , while the K-S test yields a p-value consistent with zero, meaning that the SFE distribution in the arm and bar are intrinsically different. Thus, we

<sup>6</sup> The oxygen abundance in units of  $12 + \log(\text{O}/\text{H})$

<sup>7</sup> <http://dx.doi.org/10.11570/21.0024>



observe a suppression of the SFE in the bar compared to the spiral arms.

Generally, the SFE appears rather similar in the galactic bars, disks without spirals, and inside the central regions, while it is slightly higher on average in the arm-interarm regions, as shown in the right panel of Figure 4. The SFE distributions in the arms and interarms show a somewhat different shape and peak widths, with the the K-S test showing that they are statistically different. Their median values are, however, very similar.

### 4.3 $\langle SFR_5 \rangle / \langle SFR_{200} \rangle$ distribution in the arms and interarms

Similarly as for the molecular SFE in Section 4.2, we investigated the distribution of the  $\log \langle SFR_5 \rangle / \langle SFR_{200} \rangle$  parameter in different internal galactic environments, as shown in the middle panel of Figure 4. This panel shows that the  $\langle SFR_5 \rangle / \langle SFR_{200} \rangle$  distribution in the arms and interarms covers the high distribution end very similarly, while the low distribution end is populated by the areas associated with the interarms much more. This observation is not affected by the DIG regions, as shown in the same figure.

We also performed the K-S test for  $\langle SFR_5 \rangle / \langle SFR_{200} \rangle$ , and it produced a similar result as for the SFE, albeit with a higher significance. That is in line with the previous observations for NGC 628 in Paper I. In addition to having different shapes, we also see that the arm-interarm  $\langle SFR_5 \rangle / \langle SFR_{200} \rangle$  distributions have drastically different medians.

In an attempt to understand the differences in the  $\langle SFR_5 \rangle / \langle SFR_{200} \rangle$  distribution in the arms and interarms, we looked into the global properties of the galaxies, such as the bulge-to-total light ratio (B/T) from Salo et al. (2015) and morphological type, as shown in Figure 5. Those galaxies where the median  $\langle SFR_5 \rangle / \langle SFR_{200} \rangle$  in the interarms is lower, resulting in larger differences in  $\langle SFR_5 \rangle / \langle SFR_{200} \rangle$  in the arms-interarms (dubbed different A-IA as opposed to similar A-IA), tend to have a higher B/T ratio, as opposed to the similar A-IA galaxies. Moreover, we also see that many of the similar A-IA galaxies belong to a later morphological type (Sc), again shown in Figure 5, while the majority of the different A-IA galaxies belong to the Sa and Sb type, which are characterised by a larger bulge and less prominent spiral structure compared to the Sc type. Therefore, our results also demonstrate that the galaxies with larger B/T ratios are of an earlier morphological type, which is supported by their larger bulges contributing a higher fraction of the total emitted light. We note however, that this sample size is too small to make an exhaustive conclusion about the trend.

In summary, we notice a characteristic behaviour among the galaxies in the sample where some have  $\langle SFR_5 \rangle / \langle SFR_{200} \rangle$  stretching down to lower values in the interarms and show a more distinct difference from the  $\langle SFR_5 \rangle / \langle SFR_{200} \rangle$  distribution in the arms, while other galaxies have rather similar  $\langle SFR_5 \rangle / \langle SFR_{200} \rangle$  in the same regions. The former group also tends to have galaxies with larger B/T values and an earlier morphological type.

## 5 DISCUSSION

### 5.1 Potential influences on $\langle SFR_5 \rangle / \langle SFR_{200} \rangle$

In this section, we discuss possible explanations to the observed differences between the  $\langle SFR_5 \rangle / \langle SFR_{200} \rangle$  distributions in the arms and interarms. We try to understand why the interarm regions have undergone a somewhat more diverse recent changes in the SF com-

pared to the spiral arms, as indicated by the  $\langle SFR_5 \rangle / \langle SFR_{200} \rangle$  distribution in the middle panel of Figure 4.

#### 5.1.1 Morphology and global stellar mass

As mentioned, the galaxies with lower median  $\langle SFR_5 \rangle / \langle SFR_{200} \rangle$  that also have more distinct recent SF changes in the arms-interarms tend to have larger stellar masses and earlier morphological types, as shown in Figure 5. Previous studies suggest that massive galaxies with larger bulges can have low star formation activity, as the gas can be affected by feedback or stabilised against collapse (e.g., Martig et al. 2009; Peng et al. 2010; Fang et al. 2013). The reach of these potential bulge-driven processes is, however, unclear and might have a limited effect on the interarm regions, given the scales of several kpc studied here.

In addition, Elmegreen et al. (2011) found that the contrast between arms-interarms tends to increase with later Hubble type (from flocculent to multiple arm to grand design) using NIR photometry, while Savchenko et al. (2020) observed in optical/NIR a somewhat larger arm width in grand design spirals in their analysis of these galaxy types. Another recent work by Stuber et al. (2023) who studied PHANGS-ALMA galaxies found that their classification agrees better with the optical/NIR literature definitions for grand design (67% of cases) than for multi-arm (47% of cases) galaxies. Thus, the spiral structure in earlier type galaxies tends to be more wavelength dependent. Therefore, for early-type galaxies in our sample that have lower arm-interarm contrast, narrower spiral arms, and higher wavelength dependency we may be contaminating the true  $\langle SFR_5 \rangle / \langle SFR_{200} \rangle$  signal in the arms-interarms as our morphological masks derived in the NIR are more likely to be imprecise.

#### 5.1.2 $\Sigma_{\text{mol}}$ and SFE

A potential explanation to the differences in  $\langle SFR_5 \rangle / \langle SFR_{200} \rangle$  between the two A-IA populations could be attributed to the molecular gas availability. The top histogram in right panel of Figure 3 hints at  $\Sigma_{\text{mol}}$  being shifted towards lower values in the interarms than in the arms. However, when we separate the different and similar A-IA, we do not see any conclusive differences in the  $\Sigma_{\text{mol}}$  distributions.

Regarding SFE, the right-most panel of Figure 4 illustrates that it has as similar range and shape in the arms and interarms, having almost identical median values. Thus, we cannot conclude if the differences in the recent SFHs in the arms and interarms are driven by the gas content availability or SFE. This points towards other factors preventing SF from taking place.

## 5.2 Model caveats

### 5.2.1 $A(\text{FUV})$ corrections

In addition, we investigated how the choice of a constant or a variable scaling coefficient  $k$  used for correcting FUV emission for dust extinction affects the distribution of  $\langle SFR_5 \rangle / \langle SFR_{200} \rangle$  in the arms and interarms. We used a constant  $k = 4.9$  from Leroy et al. (2019) who derived the scaling coefficient using SED fitting for a sample of  $\sim 15\,750$  galaxies at  $z = 0$ . The variable value was estimated with the Boquien et al. (2016) recipe who also performed SED fitting in CIGALE for eight nearby galaxies. Both methods are applicable for resolved studies. The distribution of the variable vs. constant  $k$  are shown in the left panel of Figure 7.

The constant value is considerably lower than the variable  $k$ , which ranges mostly between  $k = 4\text{--}12$ . This is in agreement with the

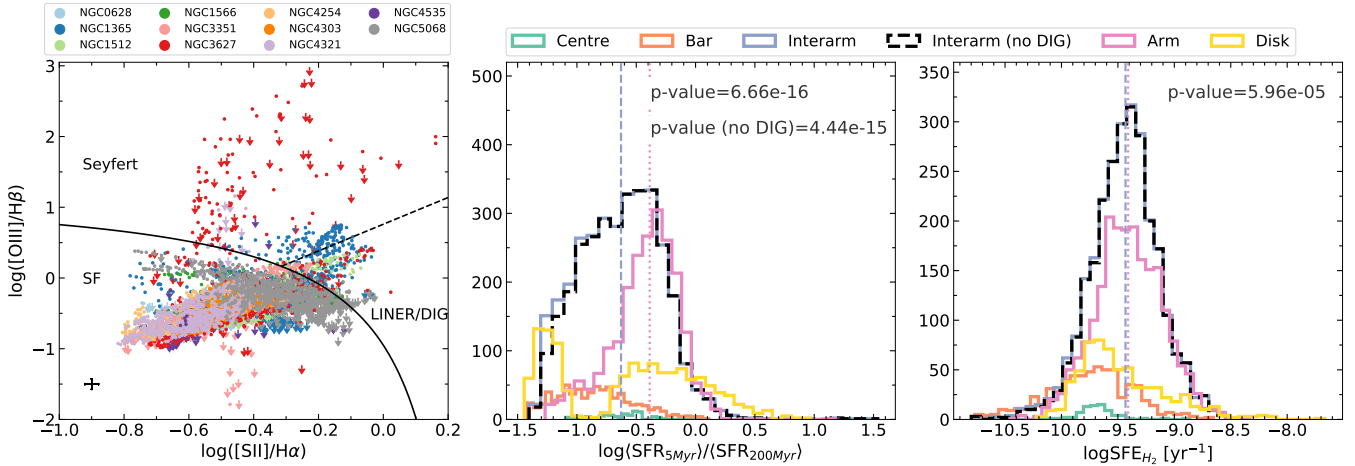


**Figure 4.** *Left panel:* the BPT diagram of the galaxies sampled used to identify the DIG regions. The error bar represents the mean uncertainty among the galaxies for the detections above the S/N cut. *Middle panel:* the  $\log\langle SFR_5 \rangle / \langle SFR_{200} \rangle$  distributions in the different internal galactic environments. The p-values are from the K-S test performed on the interarms vs. arms  $\langle SFR_5 \rangle / \langle SFR_{200} \rangle$  distributions, both for the full samples and with the DIG associated pixels excluded. The lines represent median values of the arms and interarms. *Right panel:* same as in the middle panel, but for the molecular SFE.

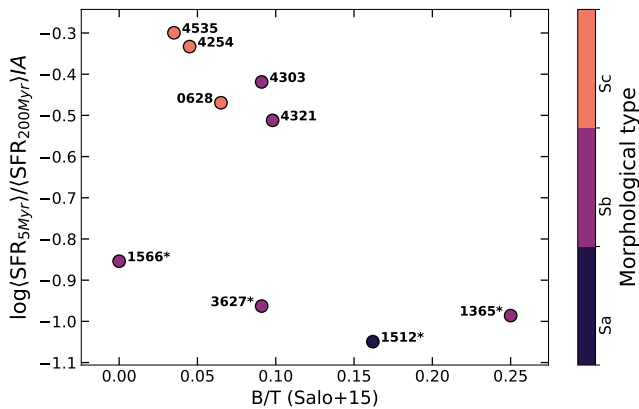


**Figure 5.** The median  $\log\langle SFR_5 \rangle / \langle SFR_{200} \rangle$  in the interarms as a function of B/T values from Salo et al. (2015), colour-coded according to the morphological type, as in Table 1, however, without a distinction between the Sb and SAb types. The galaxies with lower median  $\log\langle SFR_5 \rangle / \langle SFR_{200} \rangle$  in the interarms, i.e., those exhibiting larger differences in  $\langle SFR_5 \rangle / \langle SFR_{200} \rangle$  in the arms-interarms (marked with an asterisk), tend to be of an earlier type and have larger B/T values than the galaxies with more similar recent SFHs in the arms-interarms.

findings in Belfiore et al. (2023) who obtained a result  $\sim 0.3$  dex lower for the Leroy et al. (2019) vs. Boquien et al. (2016) recipes. As mentioned before, this could be attributed to a steeper attenuation curve in Boquien et al. (2016). Declair et al. (2019) similarly obtained a rather steep attenuation curve from SED fitting in CIGALE for NGC 628 (see their Figure 8).

Nevertheless, applying the constant value of  $k = 4.9$  has an effect on the  $\langle SFR_5 \rangle / \langle SFR_{200} \rangle$  metric as it increases the observed dynamic range of  $\langle SFR_5 \rangle / \langle SFR_{200} \rangle$ , as shown in Figure 6. This is expected because  $k$  is supposed to be enhanced in star-forming regions, as opposed to more quiescent areas where the dust is mostly heated by older stars. Thus, a constant  $k$  is likely to be larger than its true value in quiescent regions and lower in star-forming ones. Since the variable  $k$  values are mostly larger than the constant one,  $A(\text{FUV})$ , and subsequently  $L(\text{FUV})_{\text{corr}}$ , becomes lower in the latter

case, increasing  $\langle SFR_5 \rangle / \langle SFR_{200} \rangle$ . With a constant  $k$ , we observe a higher number of pixels that have experienced a recent increase in SF compared to the variable case and Paper I. That is logical, considering that on average the changes in the SFR measured on the short scales of  $\lesssim 200$  Myr over the galactic disc should be unchanged, with the total  $\langle SFR_5 \rangle / \langle SFR_{200} \rangle$  of approximately zero.

We are also interested whether the  $k$  coefficient changes the distribution of  $\langle SFR_5 \rangle / \langle SFR_{200} \rangle$  in the arms and interarms. The middle and right panels of Figure 7 show that the overall distribution of  $\langle SFR_5 \rangle / \langle SFR_{200} \rangle$  in the interarms is preserved regardless of the choice of  $k$ . Thus, we deem the use of a constant value for  $k$  a more suitable choice in our case since it reduces the systematic discrepancies between the shape of the attenuation curves used to correct for the FUV and  $H\alpha$  attenuation.

### 5.2.2 SFR measurements in faint regions

The analysis in this work relies on measurements of the SFR, and thus, assumptions made about the shape of the IMF. The interarm regions are characterised by a lower  $\Sigma_{\text{SFR}(H\alpha)}$  than the spiral arms, and since we are examining characteristic differences between the two environments, we need to ensure that these distinctions are intrinsic, rather than artefacts of the stochastic SF processes. Although we operate on physical scales much larger than the size of a typical giant molecular cloud (GMC; mostly  $\gtrsim 300$  pc per pixel as in Table 2 versus  $\sim 50$  pc, respectively), the stochasticity of the O-type SF might become important in the interarms, since there might not be enough GMCs of sufficient mass to fully populate the high-mass end of the IMF. This would lead to a systematically lower  $\text{SFR}(H\alpha)$  in the interarms as opposed to the arm regions. Moreover, considering that O-stars are very short-lived ( $\lesssim 5$  Myr), they might be missing if their original number is low, even though there was a relatively recent SF event. On the other hand, the FUV continuum emission traces OB-stars, and is therefore, less affected in this case.

Previous works have investigated systematically lower  $H\alpha$ -to-FUV ratios in dwarf galaxies, either from the integrated luminosity (Lee et al. 2009) or from fluxes (Meurer et al. 2009). Incorporating stochasticity into the SF modelling showed to produce results aligned with the observations, even for a standard Kroupa (2001) IMF (Fumagalli

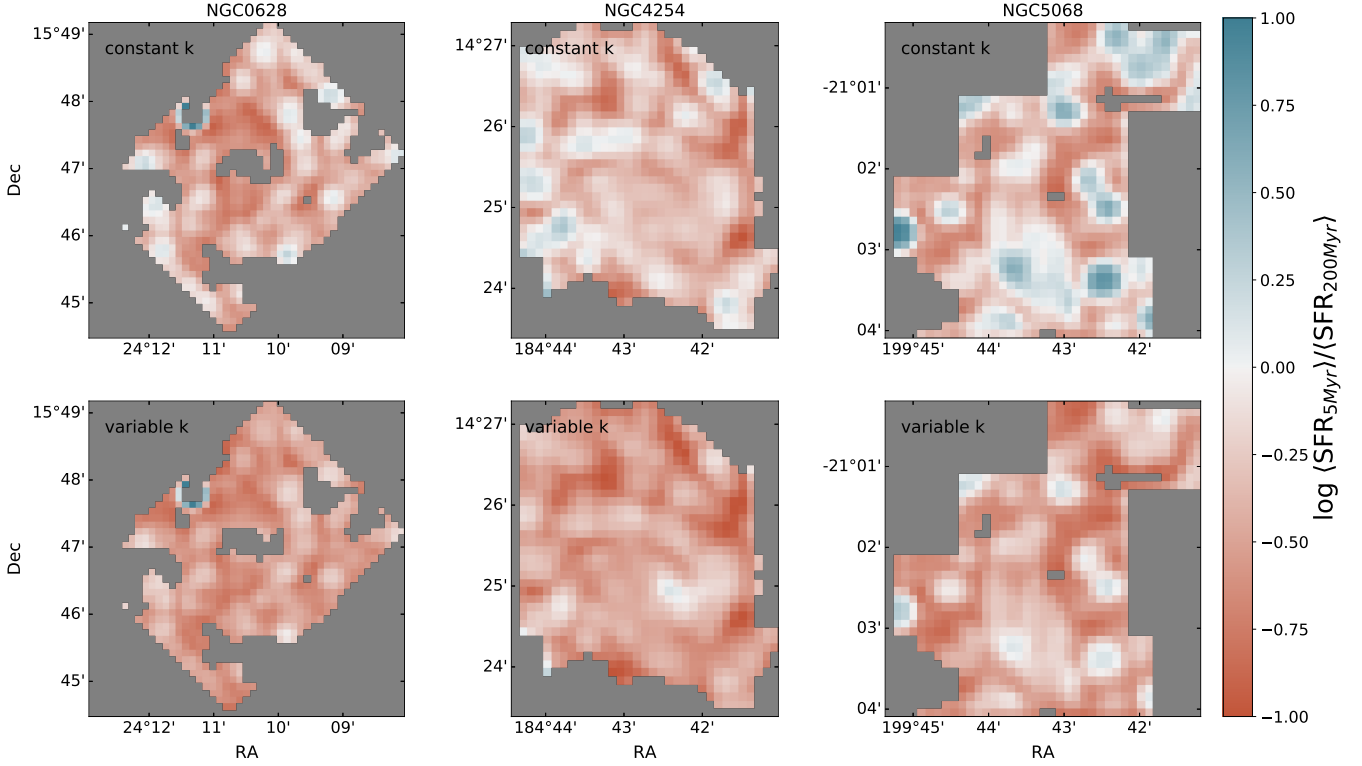


**Figure 6.** The effects on  $\langle SFR_5 \rangle / \langle SFR_{200} \rangle$  when implementing a constant  $k = 4.9$  from Leroy et al. (2019) (top row) and a variable  $k$  from Boquien et al. (2016) (bottom row) in A(FUV) calculations.

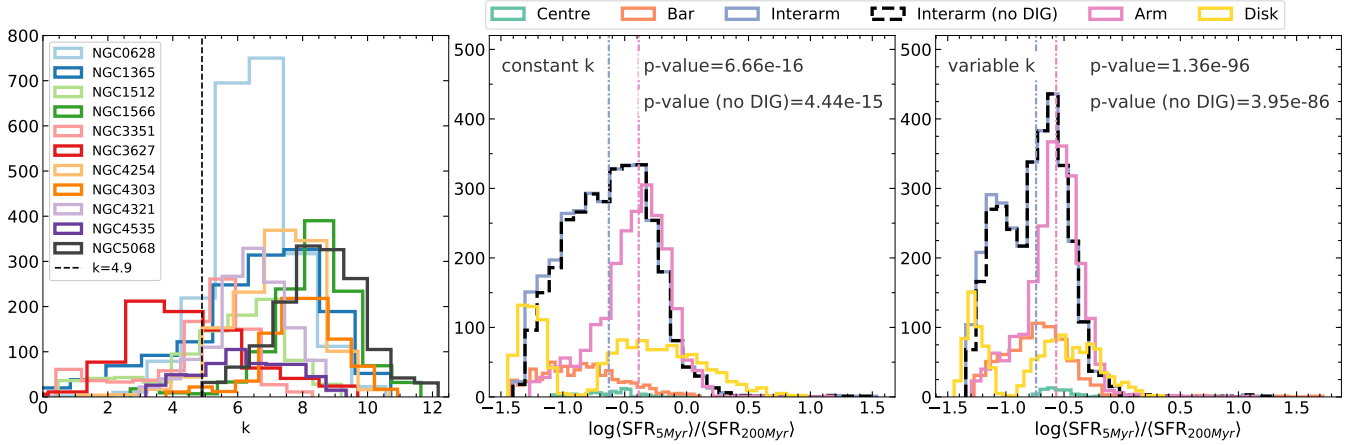


**Figure 7.** Left panel: variable  $k$  from Boquien et al. (2016) in colour vs. the constant  $k$  (dashed line) from Leroy et al. (2019). Middle panel: the logarithm of  $\langle SFR_5 \rangle / \langle SFR_{200} \rangle$  when A(FUV) is corrected assuming  $k = 4.9$  from Leroy et al. (2019). The dot-dashed lines denote median values for the arm and interarm distributions. The p-values were derived using the K-S test. Right panel: same as in the middle panel but with the variable  $k$  from Boquien et al. (2016).

et al. 2011). Given the importance of the stochasticity, it might introduce a larger uncertainty in the fainter interarm regions. To form at least one high-mass star with  $M_\star \geq 30 M_\odot$ , the mass of the stellar cluster would vary between a few  $10^4 - 10^5 M_\odot$  (e.g., Calzetti 2013). For a typical lifespan of an O-star,  $\sim 5$  Myr, this would correspond to a SFR of  $0.002 - 0.02 M_\odot \text{ yr}^{-1}$ . In our sample we do encounter pixels where the SFR is below this threshold, both in the arms and interarms, meaning that we are likely to undersample the IMF in those regions. This would lead to an increased scatter in our SFR measurements. However, it is unlikely to have a systematic effect between the

arms-interarms and cause the differences in the  $\langle SFR_5 \rangle / \langle SFR_{200} \rangle$  distribution in those regions.

In addition, both H $\alpha$  and FUV emission is susceptible to the contamination from old stellar populations (e.g., Greggio & Renzini 1990; Hernández-Pérez & Bruzual 2014; Belfiore et al. 2016; Byler et al. 2019). To test whether we are operating in a regime where the emission from old stars dominates over the young ones, we calculated the specific SFR (sSFR) in each pixel, setting a threshold of  $\log(\text{sSFR}) \leq -10.6 \text{ yr}^{-1}$ , similarly as in Hunt et al. (2019), which corresponds to the turnover in the SFMS in Salim et al. (2007) or

Saintonge & Catinella (2022), for example. We did not find any pixels where this criterion would indicate that the emission mostly comes from old stars.

In summary, we might not be able to fully sample the high-mass end of the ISM in the interarms due to the stochastic nature of the O-type SF in low  $\Sigma_{\text{SFR}(\text{H}\alpha)}$  environments. Thus, we could be introducing larger uncertainties on the measured  $\langle \text{SFR}_5 \rangle / \langle \text{SFR}_{200} \rangle$  parameter. However, any systematic shifts in the  $\langle \text{SFR}_5 \rangle / \langle \text{SFR}_{200} \rangle$  distribution in the arms and interarms are unlikely. We also did not find any pixels where the H $\alpha$  and FUV emission would be predominantly caused by old stellar populations.

### 5.3 Comparison with other works

In Paper I, we compared our  $\langle \text{SFR}_5 \rangle / \langle \text{SFR}_{200} \rangle$  to other metrics that have been used to measure recent SFR changes, including “logSFR79” from Wang & Lilly (2020) and the  $D_n(4000)$  break from Kauffmann et al. (2003). The logSFR79 diagnostic is defined using the H $\alpha$  equivalent width, the Lick index of the H $\delta$  absorption, and the 4000 Å break,  $D_n(4000)$ . This makes this index particularly sensitive to the SFR changes that have occurred during the past 5 Myr, versus 800 Myr. The  $D_n(4000)$  break, on the other hand, can indicate stellar populations younger than 1 Gyr when  $D_n(4000) < 1.5$  (Kauffmann et al. 2003). We found that there were possible scenarios that could explain the changes in the recent SFH as derived by all three metrics as they all probe different timescales. For a more in-depth discussion, see Section 5.2 and Figure 9 in Paper I.

There are, however, even more conventional SFR change tracers, such as,  $\log(\text{SFR}_{\text{H}\alpha} / \text{SFR}_{\text{FUV}})$ , that can reveal similar information about the direction of the recent SF activity. In Figure 8, we show both  $\log(\langle \text{SFR}_5 \rangle / \langle \text{SFR}_{200} \rangle)$  and  $\log(\text{SFR}_{\text{H}\alpha} / \text{SFR}_{\text{FUV}})$  for selected galaxies. Generally, we see a good agreement between both indices, however,  $\langle \text{SFR}_5 \rangle / \langle \text{SFR}_{200} \rangle$  offers a broader parameter range and is therefore better at distinguishing the strength of an increase/decrease in the SF activity. There is another interesting difference: the non-linear relationship between  $\log(\langle \text{SFR}_5 \rangle / \langle \text{SFR}_{200} \rangle)$  and  $\log(\text{SFR}_{\text{H}\alpha} / \text{SFR}_{\text{FUV}})$ , as demonstrated in Figure 9. The  $\langle \text{SFR}_5 \rangle / \langle \text{SFR}_{200} \rangle$  metric, therefore, shows that a linear decrease in  $\log(\text{SFR}_{\text{H}\alpha} / \text{SFR}_{\text{FUV}})$  does not correspond to a linear decrease in the recent SFR. During the early times of a SF event at high  $\log(\text{SFR}_{\text{H}\alpha} / \text{SFR}_{\text{FUV}})$  values,  $\langle \text{SFR}_5 \rangle / \langle \text{SFR}_{200} \rangle$  is very sensitive to the amplitude of the SFR increase, spanning a large dynamical range. When recent SF decreases at low  $\log(\text{SFR}_{\text{H}\alpha} / \text{SFR}_{\text{FUV}})$ ,  $\log(\langle \text{SFR}_5 \rangle / \langle \text{SFR}_{200} \rangle)$  does not drop constantly, but more realistically reaches a plateau.

## 6 CONCLUSIONS

In this work, we probed recent SFHs of eleven nearby disk galaxies using the  $\langle \text{SFR}_5 \rangle / \langle \text{SFR}_{200} \rangle$  metric defined in Lomaeva et al. (2022). This parameter is the ratio between the SFR averaged over 5 and 200 Myr as a function of the H $\alpha$ –FUV colour and was calibrated in CIGALE. The H $\alpha$ –FUV colour was measured using PHANGS-MUSE and GALEX observations, both corrected for the Galactic extinction and internal dust attenuation using NIR and MIR observations. We also examined molecular gas masses with PHANGS-ALMA data. The galaxies in the current sample are star-forming, nearby disks seen mostly face-on. They represent different external (field vs. group/cluster) and internal (AGN vs. inactive; barred, unbarred, and disks without spirals) properties.

(i) The  $\langle \text{SFR}_5 \rangle / \langle \text{SFR}_{200} \rangle$  diagnostic revealed a diverse behaviour in the observed galaxies. The low global stellar mass NGC 5068 showed the most active recent SF, while the barred NGC 3351 has undergone a rapid drop in the SF across the entire disk visible. NGC 628, 1365, 4254, 4303, 4321, and 4535 host both recent boosts and drops in the SF activity, with the increased recent SFR usually concentrated along the spiral arms where the molecular gas is abundant. NGC 1512, 1566, and 3627 have mostly undergone decreasing SF in the recent past.

(ii) We observe no obvious link between a particular internal environment (bar-unbarred), external environment (field vs. cluster/group), feedback (AGN vs. no AGN) and recent SF activity traced by  $\langle \text{SFR}_5 \rangle / \langle \text{SFR}_{200} \rangle$ . This points at complex gas dynamics, rather than one particular driver of the SF.

(iii) The examination of the molecular SFE revealed that it is high in NGC 5068, similarly to  $\langle \text{SFR}_5 \rangle / \langle \text{SFR}_{200} \rangle$ , as well as in the centre of NGC 1365, which is a barred galaxy with a circumnuclear ring of high SF. According to the K-S test, the SFE distributions in the arms and interarms are intrinsically different, albeit the distribution shapes and median values are rather similar.

(iv) Similarly, the  $\langle \text{SFR}_5 \rangle / \langle \text{SFR}_{200} \rangle$  distributions in the arms and interarms are statistically different as well, with the arm population peaking at higher median values. The  $\langle \text{SFR}_5 \rangle / \langle \text{SFR}_{200} \rangle$  distribution in the interarms stretches down to lower values, and these galaxies, therefore, have a more distinct  $\langle \text{SFR}_5 \rangle / \langle \text{SFR}_{200} \rangle$  value between the arms and interarms. Since this behaviour in the arms-interarms is not seen for the SFE, we conclude that this is a matter of recent SFH variations.

(v) In the galaxies with larger differences in the arm-interarm  $\langle \text{SFR}_5 \rangle / \langle \text{SFR}_{200} \rangle$  distributions (about one half of the sample), where  $\langle \text{SFR}_5 \rangle / \langle \text{SFR}_{200} \rangle$  declines more in the interarms than in the arms, we also see higher B/T ratios and earlier morphological types (Sa and Sb vs. Sc). Since the SFE and molecular gas in the arms and interarms appear to be very similar, we conclude that this behaviour of the recent SFHs is driven by other processes that impede recent SF activity in the interarms.

(vi) We also discuss potential artefacts that could cause the observed differences in the  $\langle \text{SFR}_5 \rangle / \langle \text{SFR}_{200} \rangle$  in the arms-interarms. First, we examine the effects of variable and constant values of the scaling coefficient  $k$  used for correcting for the FUV attenuation. This does not impact the results in a significant manner. We also discuss that we might not be able to fully sample the high-mass end of the IMF in the interarms, which would introduce larger uncertainties and increase the scatter in the SFR measurements. However, we do not expect this to cause any systematic offsets. In addition, we calculated the sSFR and found that the emission from old stellar populations is not sufficient in any of the pixels to contaminate our H $\alpha$  and FUV measurements.

Generally, this work is an extension of the initial analysis performed on NGC 628 in Lomaeva et al. (2022). It proves that the  $\langle \text{SFR}_5 \rangle / \langle \text{SFR}_{200} \rangle$  metric is a useful tool for probing and comparing recent SFHs between low redshift galaxies on resolved scales. The current sample of eleven galaxies could be extended further as it was merely limited by the availability of the optical and IR data.

## ACKNOWLEDGEMENTS

We thank the anonymous referee for the comments that significantly improved the quality of the paper. IDL acknowledges support from ERC starting grant #851622 DustOrigin. This research has made use of the SIMBAD database, operated at CDS, Strasbourg, France. Pack-

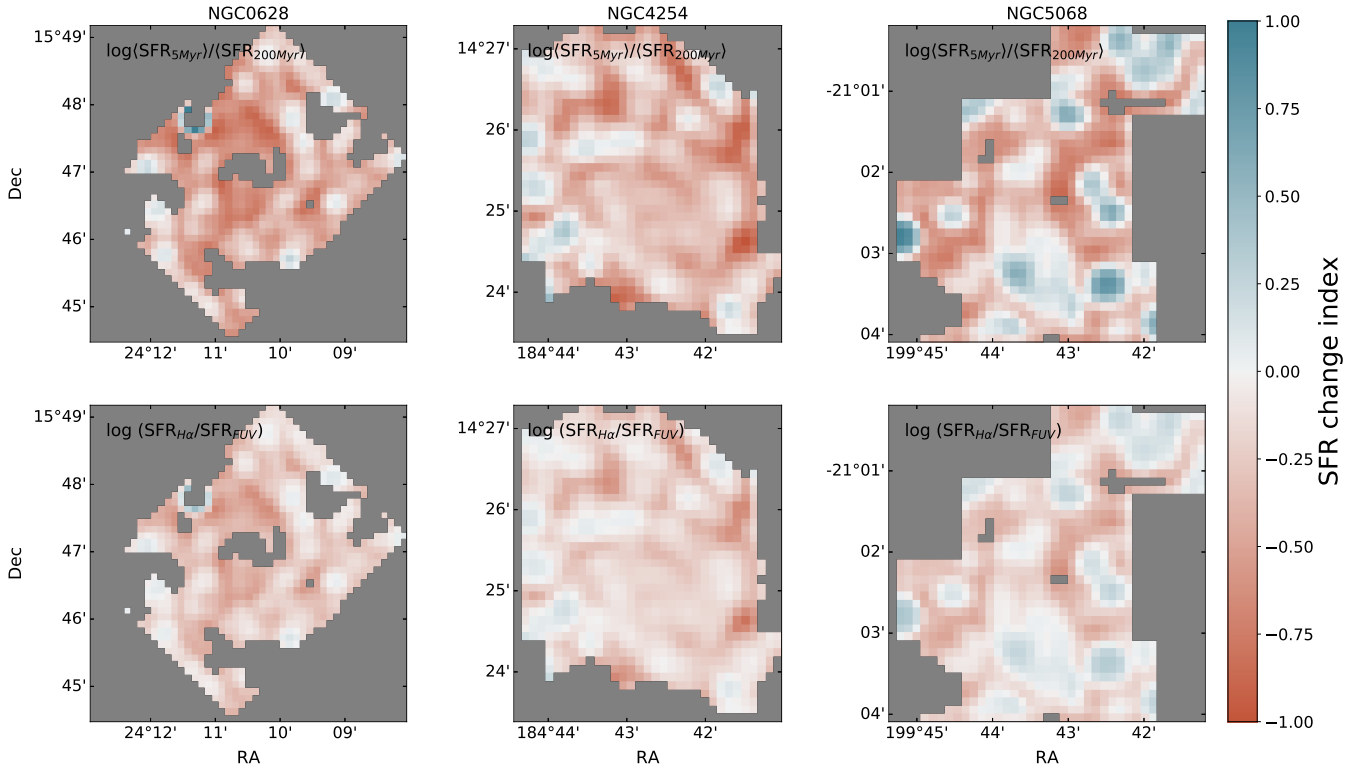


**Figure 8.** The comparison between  $\langle SFR_5 \rangle / \langle SFR_{200} \rangle$  (top row) and  $\log(SFR_{H\alpha} / SFR_{FUV})$  (bottom row) for a selection of galaxies. Both metrics were obtained using attenuation corrected  $H\alpha$  and FUV observations.

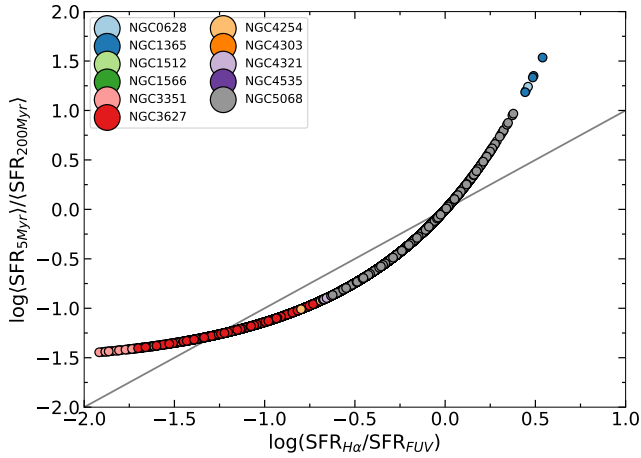


**Figure 9.** The comparison between the observed  $\log(\langle SFR_5 \rangle / \langle SFR_{200} \rangle)$  and  $\log(SFR_{H\alpha} / SFR_{FUV})$  with the solid line showing the one-to-one relation. Again, both metrics were obtained using attenuation corrected  $H\alpha$  and FUV observations.

ages used and not cited in the main text: seaborn (Waskom 2021); montage is funded by the National Science Foundation under Grant Number ACI-1440620, and was previously funded by the National Aeronautics and Space Administration’s Earth Science Technology Office, Computation Technologies Project, under Cooperative Agreement Number NCC5-626 between NASA and the California Institute of Technology.

## DATA AVAILABILITY

The data used in this article are publicly available through the PHANGS-MUSE, PHANGS-ALMA, the NED and DustPedia databases; any additional data will be shared upon reasonable request to the corresponding author.

## REFERENCES

- Abadi M. G., Moore B., Bower R. G., 1999, *MNRAS*, **308**, 947  
 Accurso G., et al., 2017, *MNRAS*, **470**, 4750  
 Aguerri J. A. L., Balcells M., Peletier R. F., 2001, *A&A*, **367**, 428  
 Alloin D., Nieto J. L., 1982, *A&AS*, **50**, 491  
 Alonso-Herrero A., Knapen J. H., 2001, *AJ*, **122**, 1350  
 Alston W. N., et al., 2021, *MNRAS*, **505**, 3722  
 Amorín R., Muñoz-Tuñón C., Aguerri J. A. L., Planesas P., 2016, *A&A*, **588**, A23  
 Anand G. S., et al., 2021, *MNRAS*, **501**, 3621  
 Astropy Collaboration et al., 2013, *A&A*, **558**, A33  
 Astropy Collaboration et al., 2018, *AJ*, **156**, 123  
 Athanassoula E., Machado R. E. G., Rodionov S. A., 2013, *MNRAS*, **429**, 1949  
 Bacon R., et al., 2010, in McLean I. S., Ramsay S. K., Takami H., eds, Society of Photo-Optical Instrumentation Engineers (SPIE) Conference Series Vol. 7735, Ground-based and Airborne Instrumentation for Astronomy III, p. 773508, doi:10.1117/12.856027  
 Bacon R., Piqueras L., Conseil S., Richard J., Shepherd M., 2016, MPA/DAF: MUSE Python Data Analysis Framework (ascl:1611.003)  
 Baldwin J. A., Phillips M. M., Terlevich R., 1981, *PASP*, **93**, 5  
 Balogh M. L., Morris S. L., 2000, *MNRAS*, **318**, 703  
 Balogh M. L., Navarro J. F., Morris S. L., 2000, *ApJ*, **540**, 113  
 Bekki K., 1998, *ApJ*, **502**, L133  
 Belfiore F., Maiolino R., Bothwell M., 2016, *MNRAS*, **455**, 1218

- Belfiore F., et al., 2023, *A&A*, 670, A67
- Binggeli B., Sandage A., Tammann G. A., 1985, *AJ*, 90, 1681
- Bolatto A. D., Wolfire M., Leroy A. K., 2013, *ARA&A*, 51, 207
- Boquien M., et al., 2016, *A&A*, 591, A6
- Boquien M., Burgarella D., Roehlly Y., Buat V., Ciesla L., Corre D., Inoue A. K., Salas H., 2019, *A&A*, 622, A103
- Boselli A., et al., 2016, *A&A*, 596, A11
- Boselli A., et al., 2018a, *A&A*, 615, A114
- Boselli A., et al., 2018b, *A&A*, 615, A114
- Boselli A., et al., 2021, *A&A*, 646, A139
- Boselli A., Fossati M., Sun M., 2022, *A&ARv*, 30, 3
- Bradley L., et al., 2020, *astropy/photutils*: 1.0.0, doi:10.5281/zenodo.4044744, <https://doi.org/10.5281/zenodo.4044744>
- Broussard A., et al., 2019, *ApJ*, 873, 74
- Bruzual G., Charlot S., 2003, *MNRAS*, 344, 1000
- Bundy K., et al., 2010, *ApJ*, 719, 1969
- Burgarella D., Buat V., Iglesias-Páramo J., 2005, *MNRAS*, 360, 1413
- Burtscher L., et al., 2021, *A&A*, 654, A132
- Byler N., Dalcanton J. J., Conroy C., Johnson B. D., Choi J., Dotter A., Rosenfield P., 2019, *AJ*, 158, 2
- Byun W., et al., 2021, *ApJ*, 918, 82
- Calzetti D., 2013, *Star Formation Rate Indicators*, p. 419
- Calzetti D., Kinney A. L., Storchi-Bergmann T., 1994, *ApJ*, 429, 582
- Calzetti D., Armus L., Bohlin R. C., Kinney A. L., Koornneef J., Storchi-Bergmann T., 2000, *ApJ*, 533, 682
- Cardelli J. A., Clayton G. C., Mathis J. S., 1989, *ApJ*, 345, 245
- Carnall A. C., Leja J., Johnson B. D., McLure R. J., Dunlop J. S., Conroy C., 2019, *The Astrophysical Journal*, 873, 44
- Catalán-Torrecilla C., et al., 2017, *ApJ*, 848, 87
- Cepa J., Beckman J. E., 1990, *ApJ*, 349, 497
- Ceverino D., Dekel A., Bournaud F., 2010, *MNRAS*, 404, 2151
- Chabrier G., 2003, *PASP*, 115, 763
- Chen Y.-M., Tremonti C. A., Heckman T. M., Kauffmann G., Weiner B. J., Brinchmann J., Wang J., 2010, *AJ*, 140, 445
- Chown R., et al., 2019, *MNRAS*, 484, 5192
- Ciesla L., et al., 2016, *A&A*, 585, A43
- Ciesla L., Elbaz D., Fensch J., 2017, *A&A*, 608, A41
- Colina L., Vargas M. L. G., Mas-Hesse J. M., Alberdi A., Krabbe A., 1997, *The Astrophysical Journal*, 484, L41
- Combes F., et al., 2014, *A&A*, 565, A97
- Conroy C., 2013, *Annual Review of Astronomy and Astrophysics*, 51, 393
- Croton D. J., et al., 2006, *MNRAS*, 365, 11
- Declair M., et al., 2019, *Monthly Notices of the Royal Astronomical Society*, 486, 743
- Dekel A., Birnboim Y., 2006, *MNRAS*, 368, 2
- Di Matteo T., Springel V., Hernquist L., 2005, *Nature*, 433, 604
- Díaz-García S., et al., 2021, *A&A*, 654, A135
- Ducci L., Kavanagh P. J., Sasaki M., Koribalski B. S., 2014, *A&A*, 566, A115
- Ellison S. L., Nair P., Patton D. R., Scudder J. M., Mendel J. T., Simard L., 2011, *MNRAS*, 416, 2182
- Elmegreen B. G., 1994, *ApJ*, 433, 39
- Elmegreen B. G., Elmegreen D. M., 1983, *MNRAS*, 203, 31
- Elmegreen D. M., et al., 2011, *ApJ*, 737, 32
- Emami N., Siana B., Weisz D. R., Johnson B. D., Ma X., El-Badry K., 2019, *ApJ*, 881, 71
- Emsellem E., et al., 2022, *A&A*, 659, A191
- Engel H., et al., 2010, *ApJ*, 724, 233
- Faist A. L., Capak P. L., Emami N., Tacchella S., Larson K. L., 2019, *ApJ*, 884, 133
- Fang J. J., Faber S. M., Salim S., Graves G. J., Rich R. M., 2012, *ApJ*, 761, 23
- Fang J. J., Faber S. M., Koo D. C., Dekel A., 2013, *ApJ*, 776, 63
- Fazio G. G., et al., 2004, *ApJS*, 154, 10
- Ferrarese L., et al., 2000, *ApJS*, 128, 431
- Flores Velázquez J. A., et al., 2021, *MNRAS*, 501, 4812
- Fouque P., Gourgoulhon E., Chamaraux P., Paturel G., 1992, *A&AS*, 93, 211
- Foyle K., Rix H. W., Walter F., Leroy A. K., 2010, *ApJ*, 725, 534
- Fumagalli M., da Silva R. L., Krumholz M. R., 2011, *ApJ*, 741, L26
- Gadotti D. A., et al., 2019, *MNRAS*, 482, 506
- Gaibler V., Khochfar S., Krause M., Silk J., 2012, *MNRAS*, 425, 438
- Gallazzi A., Bell E. F., 2009, *The Astrophysical Journal Supplement Series*, 185, 253
- Gao Y., Egusa F., Liu G., Kohno K., Bao M., Morokuma-Matsui K., Kong X., Chen X., 2021, *ApJ*, 913, 139
- García A. M., 1993, *A&AS*, 100, 47
- Greggio L., Renzini A., 1990, *ApJ*, 364, 35
- Groves B., et al., 2023, *MNRAS*, 520, 4902
- Gunn J. E., Gott J. Richard I., 1972, *ApJ*, 176, 1
- Guo Y., et al., 2016, *ApJ*, 833, 37
- Haynes M. P., Giovanelli R., Roberts M. S., 1979, *ApJ*, 229, 83
- Heckman T. M., Best P. N., 2014, *ARA&A*, 52, 589
- Hernández-Pérez F., Bruzual G., 2014, *MNRAS*, 444, 2571
- Hernquist L., Mihos J. C., 1995, *ApJ*, 448, 41
- Herrera C. N., et al., 2020, *A&A*, 634, A121
- Ho L. C., Filippenko A. V., Sargent W. L. W., 1997, *The Astrophysical Journal Supplement Series*, 112, 315
- Hopkins P. F., Hernquist L., Cox T. J., Di Matteo T., Robertson B., Springel V., 2006, *ApJS*, 163, 1
- Hunt L. K., et al., 2008, *A&A*, 482, 133
- Hunt L. K., et al., 2019, *A&A*, 621, A51
- Iles E. J., Pettitt A. R., Okamoto T., 2022, *MNRAS*, 510, 3899
- Ishibashi W., Fabian A. C., 2012, *MNRAS*, 427, 2998
- Jogee S., Scoville N., Kenney J. D. P., 2005, *ApJ*, 630, 837
- Kalfountzou E., et al., 2017, *MNRAS*, 471, 28
- Kamphuis J., Briggs F., 1992, *A&A*, 253, 335
- Karachentsev I. D., et al., 2002, *A&A*, 385, 21
- Karachentsev I. D., Kaisina E. I., Kaisin S. S., 2021, *MNRAS*, 506, 1346
- Kauffmann G., et al., 2003, *MNRAS*, 341, 33
- Kaviraj S., Peirani S., Khochfar S., Silk J., Kay S., 2009, *MNRAS*, 394, 1713
- Kennicutt R. C., Evans N. J., 2012, *Annual Review of Astronomy and Astrophysics*, 50, 531
- Kennicutt R. C., et al., 2011, *PASP*, 123, 1347
- Kereš D., Katz N., Weinberg D. H., Davé R., 2005, *MNRAS*, 363, 2
- Kewley L. J., Dopita M. A., Sutherland R. S., Heisler C. A., Trevena J., 2001, *ApJ*, 556, 121
- Kewley L. J., Groves B., Kauffmann G., Heckman T., 2006, *MNRAS*, 372, 961
- Khoperskov S., Haywood M., Di Matteo P., Lehnert M. D., Combes F., 2018, *A&A*, 609, A60
- Kilborn V. A., Koribalski B. S., Forbes D. A., Barnes D. G., Musgrave R. C., 2005, *MNRAS*, 356, 77
- Kim S. S., Saitoh T. R., Jeon M., Figer D. F., Merritt D., Wada K., 2011, *The Astrophysical Journal Letters*, 735, L11
- Kim W.-T., Kim C.-G., Ostriker E. C., 2020, *ApJ*, 898, 35
- Knapen J. H., Cepa J., Beckman J. E., Soledad del Río M., Pedlar A., 1993, *ApJ*, 416, 563
- Knapen J. H., Beckman J. E., Cepa J., Nakai N., 1996, *A&A*, 308, 27
- Koribalski B. S., López-Sánchez Á. R., 2009, *MNRAS*, 400, 1749
- Kreckel K., Blanc G. A., Schinnerer E., Groves B., Adamo A., Hughes A., Meidt S., 2016, *ApJ*, 827, 103
- Kroupa P., 2001, *MNRAS*, 322, 231
- Lang P., et al., 2020, *ApJ*, 897, 122
- Larson R. B., 1974, *Monthly Notices of the Royal Astronomical Society*, 169, 229
- Leaman R., et al., 2019, *MNRAS*, 488, 3904
- Lee J. C., et al., 2009, *ApJ*, 706, 599
- Leja J., Carnall A. C., Johnson B. D., Conroy C., Speagle J. S., 2019, *ApJ*, 876, 3
- Lemonias J. J., et al., 2011, *ApJ*, 733, 74
- Leroy A. K., et al., 2019, *ApJS*, 244, 24
- Leroy A. K., et al., 2021a, arXiv e-prints, p. arXiv:2104.07665
- Leroy A. K., et al., 2021b, arXiv e-prints, p. arXiv:2104.07739
- Lindblad P. O., 1999, *A&ARv*, 9, 221
- Liu J.-F., Bregman J. N., Lloyd-Davies E., Irwin J., Espaillat C., Seitzer P., 2005, *The Astrophysical Journal*, 621, L17

- Lomaeva M., De Looze I., Saintonge A., Declair M., 2022, *MNRAS*, **517**, 3763
- Lord S. D., Young J. S., 1990, *ApJ*, **356**, 135
- Ma C., de Grijs R., Ho L. C., 2017, *ApJS*, **230**, 14
- Ma C., de Grijs R., Ho L. C., 2018, *ApJ*, **857**, 116
- Madden S. C., et al., 2020, *A&A*, **643**, A141
- Maeda F., Ohta K., Fujimoto Y., Habe A., Ushio K., 2020, *MNRAS*, **495**, 3840
- Maeda F., Egusa F., Ohta K., Fujimoto Y., Habe A., 2023, *ApJ*, **943**, 7
- Maia M. A. G., da Costa L. N., Latham D. W., 1989, *ApJS*, **69**, 809
- Martig M., Bournaud F., Teyssier R., Dekel A., 2009, *ApJ*, **707**, 250
- Martin D. C., et al., 2005, *The Astrophysical Journal*, 619, L1
- Mercedes-Feliz J., et al., 2023, *arXiv e-prints*, p. arXiv:2301.01784
- Meurer G. R., et al., 2009, *ApJ*, **695**, 765
- Momose R., Okumura S. K., Koda J., Sawada T., 2010, *ApJ*, **721**, 383
- Morrissey P., et al., 2007, *ApJS*, **173**, 682
- Muraoka K., et al., 2019, *PASJ*, **71**, S15
- Muzzin A., Marchesini D., van Dokkum P. G., Labbé I., Kriek M., Franx M., 2009, *ApJ*, **701**, 1839
- Newnham L., Hess K. M., Masters K. L., Kruk S., Penny S. J., Lingard T., Smethurst R. J., 2020, *MNRAS*, **492**, 4697
- Noeske K. G., et al., 2007, *ApJ*, **660**, L43
- Noll S., Burgarella D., Giovannoli E., Buat V., Marcellac D., Muñoz-Mateos J. C., 2009, *A&A*, **507**, 1793
- O'Donnell J. E., 1994, *ApJ*, **422**, 158
- Oevirk P., Pichon C., Lançon A., Thiébaud E., 2006, *Monthly Notices of the Royal Astronomical Society*, **365**, 46
- Osterbrock D. E., Ferland G. J., 2006, *Astrophysics of gaseous nebulae and active galactic nuclei*
- Papovich C., Dickinson M., Ferguson H. C., 2001, *ApJ*, **559**, 620
- Peng Y.-j., et al., 2010, *ApJ*, **721**, 193
- Piqueras L., Conseil S., Shepherd M., Bacon R., Leclercq F., Richard J., 2019, in Molinaro M., Shortridge K., Pasian F., eds, *Astronomical Society of the Pacific Conference Series Vol. 521, Astronomical Data Analysis Software and Systems XXVI*. p. 545
- Querejeta M., et al., 2021, *arXiv e-prints*, p. arXiv:2109.04491
- Quilis V., Moore B., Bower R., 2000, *Science*, **288**, 1617
- Rieke G. H., et al., 2004, *ApJS*, **154**, 25
- Saintonge A., Catinella B., 2022, *arXiv e-prints*, p. arXiv:2202.00690
- Saintonge A., et al., 2012, *ApJ*, **758**, 73
- Sakamoto K., Okumura S. K., Ishizuki S., Scoville N. Z., 1999, *ApJ*, **525**, 691
- Salim S., et al., 2007, *ApJS*, **173**, 267
- Salim S., et al., 2016, *ApJS*, **227**, 2
- Salim S., Boquien M., Lee J. C., 2018, *ApJ*, **859**, 11
- Salo H., et al., 2015, *ApJS*, **219**, 4
- Sanders D. B., Mirabel I. F., 1996, *ARA&A*, **34**, 749
- Savchenko S., Marchuk A., Mosenkov A., Grishunin K., 2020, *MNRAS*, **493**, 390
- Schinnerer E., et al., 2017, *ApJ*, **836**, 62
- Schinnerer E., et al., 2023, *ApJ*, **944**, L15
- Schlaflly E. F., Finkbeiner D. P., 2011, *ApJ*, **737**, 103
- Seigar M. S., James P. A., 2002, *MNRAS*, **337**, 1113
- Shapley A. E., Steidel C. C., Adelberger K. L., Dickinson M., Giavalisco M., Pettini M., 2001, *ApJ*, **562**, 95
- Sheth K., Vogel S. N., Regan M. W., Thornley M. D., Teuben P. J., 2005, *ApJ*, **632**, 217
- Shin J., Kim S. S., Baba J., Saitoh T. R., Hwang J.-S., Chun K., Hozumi S., 2017, *ApJ*, **841**, 74
- Shin J., Woo J.-H., Chung A., Baek J., Cho K., Kang D., Bae H.-J., 2019, *ApJ*, **881**, 147
- Shlosman I., Begelman M. C., Frank J., 1990, *Nature*, **345**, 679
- Shobbrook R. R., 1966, *MNRAS*, **131**, 293
- Silk J., Nusser A., 2010, *ApJ*, **725**, 556
- Skrutskie M. F., et al., 2006, *The Astrophysical Journal*, **131**, 1163
- Sparre M., Hayward C. C., Feldmann R., Faucher-Giguère C.-A., Muratov A. L., Kereš D., Hopkins P. F., 2017, *MNRAS*, **466**, 88
- Stuber S. K., et al., 2023, *A&A*, **676**, A113
- Sullivan M., Treyer M. A., Ellis R. S., Bridges T. J., Milliard B., Donas J., 2000, *MNRAS*, **312**, 442
- Tacchella S., Dekel A., Carollo C. M., Ceverino D., DeGraf C., Lapiner S., Mandelker N., Primack Joel R., 2016, *MNRAS*, **457**, 2790
- Veilleux S., Kim D. C., Sanders D. B., 2002, *ApJS*, **143**, 315
- Véron-Cetty M. P., Véron P., 2006, *A&A*, **455**, 773
- Vogel S. N., Kulkarni S. R., Scoville N. Z., 1988, *Nature*, **334**, 402
- Vollmer B., Huchtmeier W., van Driel W., 2005, *A&A*, **439**, 921
- Wang E., Lilly S. J., 2020, *ApJ*, **892**, 87
- Wang J., et al., 2012, *MNRAS*, **423**, 3486
- Wang J., Athanassoula E., Yu S.-Y., Wolf C., Shao L., Gao H., Randriamampandry T. H., 2020, *ApJ*, **893**, 19
- Waskom M. L., 2021, *Journal of Open Source Software*, **6**, 3021
- Weisz D. R., et al., 2012, *ApJ*, **744**, 44
- Wenger M., et al., 2000, *A&AS*, **143**, 9
- Werner M. W., et al., 2004, *The Astrophysical Journal Supplement Series*, **154**, 1
- Weżgowiec M., Urbanik M., Vollmer B., Beck R., Chyży K. T., Soida M., Balkowski C., 2007, *A&A*, **471**, 93
- Weżgowiec M., Beck R., Hanasz M., Soida M., Ehle M., Dettmar R. J., Urbanik M., 2022, *A&A*, **665**, A64
- Wolf C., Golding J., Onken C. A., Shao L., 2019, *arXiv e-prints*, p. arXiv:1904.08612
- Wozniak H., Friedli D., Martinet L., Pfnninger D., 1999, in Cox P., Kessler M., eds, *ESA Special Publication Vol. 427, The Universe as Seen by ISO*. p. 989
- Wuyts S., et al., 2011, *The Astrophysical Journal*, **742**, 96
- Young J. S., Allen L., Kenney J. D. P., Lesser A., Rownd B., 1996, *AJ*, **112**, 1903
- Yu S.-Y., Ho L. C., 2020, *ApJ*, **900**, 150
- Yu S.-Y., Ho L. C., Wang J., 2021, *ApJ*, **917**, 88
- Zee W.-B. G., Paudel S., Moon J.-S., Yoon S.-J., 2023, *ApJ*, **949**, 91
- Zibetti S., Charlot S., Rix H.-W., 2009, *Monthly Notices of the Royal Astronomical Society*, **400**, 1181
- den Brok J. S., et al., 2021, *MNRAS*, **504**, 3221
- van der Wel A., et al., 2014, *The Astrophysical Journal*, **788**, 28

This paper has been typeset from a  $\text{\TeX}/\text{\LaTeX}$  file prepared by the author.